JPL Publication 95-14

Microwave Resonator Measurements of Atmospheric Absorption Coefficients: A Preliminary Design Study

Steven J. Walter
Thomas R. Spilker

August 3, 1995

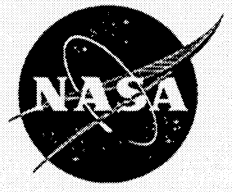

National Aeronautics and
Space Administration
by

Jet Propulsion Laboratory
California Institute of Technology
Pasadena, California

JPL Publication 95-14

Microwave Resonator Measurements of Atmospheric Absorption Coefficients: A Preliminary Design Study

Steven J. Walter
Thomas R. Spilker

August 3, 1995

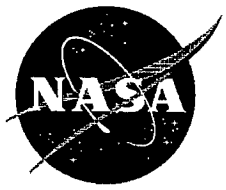

National Aeronautics and
Space Administration
by

Jet Propulsion Laboratory
California Institute of Technology
Pasadena, California

The research described in this publication was carried out by the Jet Propulsion Laboratory, California Institute of Technology, under a contract with the National Aeronautics and Space Administration.

ABSTRACT

A preliminary design study examined the feasibility of using microwave resonator measurements to improve the accuracy of atmospheric absorption coefficients and refractivity between 18 and 35 GHz. Increased accuracies would improve the capability of water vapor radiometers to correct for radio signal delays caused by Earth's atmosphere. Calibration of delays incurred by radio signals traversing the atmosphere has applications to both deep space tracking and planetary radio science experiments. Currently, the Cassini gravity wave search requires 0.8–1.0% absorption coefficient accuracy.

This study examined current atmospheric absorption models and estimated that current model accuracy ranges from 5% to 7%. The refractivity of water vapor is known to 1% accuracy, while the refractivity of many dry gases (oxygen, nitrogen, etc.) are known to better than 0.1%. Improvements to the current generation of models will require that both the functional form and absolute absorption of the water vapor spectrum be calibrated and validated.

Several laboratory techniques for measuring atmospheric absorption and refractivity were investigated, including absorption cells, single and multimode rectangular cavity resonators, and Fabry-Perot resonators. Semi-confocal Fabry-Perot resonators were shown to provide the most cost-effective and accurate method of measuring atmospheric gas refractivity. The need for accurate environmental measurement and control was also addressed. A preliminary design for the environmental control and measurement system was developed to aid in identifying significant design issues.

The analysis indicated that overall measurement accuracy will be limited by measurement errors and imprecise control of the gas sample's thermodynamic state, thermal expansion and vibration-induced deformation of the resonator structure, and electronic measurement error. The central problem is to identify systematic errors because random errors can be reduced by averaging. Calibrating the resonator measurements by checking the refractivity of dry gases which are known to better than 0.1% provides a method of controlling the systematic errors to 0.1%. The primary source of error in absorptivity and refractivity measurements is thus the ability to measure the concentration of water vapor in the resonator path. Over the whole thermodynamic range of interest the accuracy of water vapor measurement is 1.5%. However, over the range responsible for most of the radio delay (i.e. conditions in the bottom two kilometers of the atmosphere) the accuracy of water vapor measurements ranges from 0.5% to 1.0%. Therefore the precision of the resonator measurements could be held to 0.3% and the overall absolute accuracy of resonator-based absorption and refractivity measurements will range from 0.6% to 1.1%.

Table of Contents

Illustrations

Tables

I. Introduction

The capability to sense atmospheric water vapor has applications to deep space tracking and planetary science. Tropospheric water vapor is a significant source of variations in the transit time of signals propagating between earth and planetary spacecraft. Consequently, the atmosphere sets limits on both sensitivity and accuracy of spacecraft-based gravitational wave searches, very long baseline interferometry (VLBI) measurements, and spacecraft occultations of planetary atmospheres.

Water vapor radiometry can be used to determine vapor-induced propagation delays [1]. Line-of-sight measurements of water vapor column density can be made using radiometric measurements of both the 22 GHz atmospheric water vapor emissions and 30 GHz atmospheric window emissions. The vapor column density allows the induced propagation delay to be calculated. Radiometric measurements have several advantages over other techniques, including potential for high instrumental accuracies, insensitivity to variations in both weather and solar illumination, and minimal radiative transfer corrections.

Retrieval of water vapor-induced path delays requires a model relating radiometric observables to the atmospheric vapor-induced propagation delay. The accuracy of path delay retrievals derived from water vapor radiometer (WVR) data is often limited by the tropospheric emission models. Unfortunately, the theoretical basis for modeling vapor emissions is inadequate to provide the requisite model accuracy. In addition to individual spectral lines, water vapor has a broad characteristic frequency-squared emission spectrum which necessitates an empirical continuum term in the emission models. The combination of an incomplete theoretical understanding and a sparsity of relevant experimental data currently restricts vapor emission model accuracy.

Spectra illustrating clear-sky atmospheric attenuation and refractivity between 15 and 35 GHz are presented in Figures 1 and 2. The absorption spectrum is dominated by the collisional-broadened, 22.235 GHz water vapor spectral line superimposed upon water vapor and oxygen continuums.

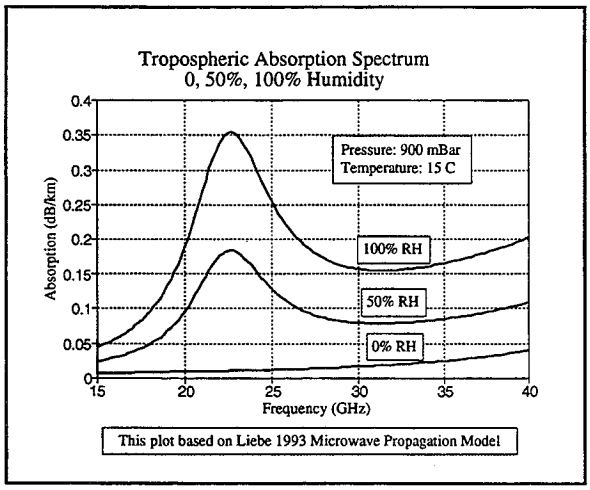

Figure 1. *Typical Absorption Spectra at 0, 50, and 100 Percent Humidity*

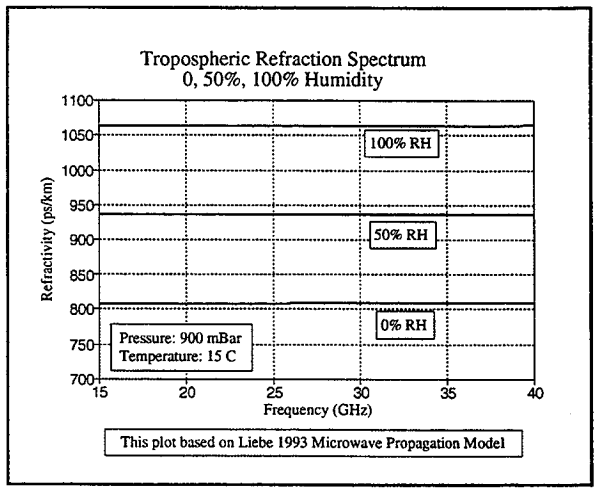

Figure 2. *Typical Refraction Spectra at 0, 50, and 100 Percent Humidity*

The structure in the absorption spectra provides contrast to the refraction spectra, which are virtually featureless. Current emission model accuracy is estimated at 4 to 7% for frequencies used for water vapor radiometry. It is inadequate to meet future needs of the Deep Space Network (DSN) where there are requirements to reduce the effect of atmospheric path delays to the picosecond-level accuracy [2]. These requirements translate into an absorption/emission model accuracy ranging from 1% to 5%, depending on the total vapor burden.

New measurements of atmospheric absorption between 15 and 40 GHz are required to improve current vapor absorption models. To resolve the existing uncertainties necessitates both measuring of the frequency, temperature, and pressure dependence of water vapor absorption and performing an absolute calibration of the total absorption. Validation of the spectral shape includes verifying the functional form of each spectral parameter including linewidth, the line shape, and continuum. The existing database of precision absorption and emission measurements needs to be significantly expanded with data representing a wide range of frequencies and meteorological conditions. Techniques for augmenting the measurement database include multi-frequency atmospheric radiometer measurements and laboratory spectrometer measurements. Absolute calibration requires that microwave absorption and/or emission measurements be made in conjunction with independent measurements of the water vapor content. Techniques for determining vapor density include comparisons with radiosondes, microwave/optical refraction measurements, infrared absorption measurements, stochastic atmospheric models developed from VLBI and Global Positioning System (GPS) measurements, and laboratory spectrometer measurements.

Laboratory spectrometer measurements have the benefit of both providing absolute calibration and being able to elucidate the water vapor spectrum dependence on frequency, pressure, and temperature. Several spectrometers were studied including single- and double-pass absorption cells, Fabry-Perot resonators, and cavity resonators. Resonator-based spectrometers infer absorption from the change in Q or bandwidth of a gas-filled resonant cavity. Therefore, resonators can use frequency or amplitude measurements to determine absorptivity. Shifts in resonance frequencies allow refractivities to be measured simultaneously with the absorption [3].

The last set of comprehensive laboratory absorption measurements of 18 to 35 GHz water vapor and oxygen absorption were made in the mid-1940s by Becker and Autler [4]. Their measurements, made at Columbia University, used an approximately cubic, 15.8 m^3, multimode cavity. The cavity was pumped at 11 frequencies from 17.8 to 40 GHz with 0.25 to 0.5 μs pulses and peak powers ranging from 10 to 40 kW. Their final data set consisted of 66 absorption measurements made at 45 °C, sea level pressure, and a humidity range spanning 0 to 50 g/m^3. Their estimate of probable error was ±5% for measurements made with "high values of attenuation," and doesn't exceed 10% for the whole data set. The fact that these measurements have not been replicated in the nearly five intervening decades is a testament to their difficulty. Recent improvements to the water vapor spectral model have come from a combination of concurrent radiosonde and water vapor radiometer measurements, theoretical improvements, and absorption measurements at millimeter-wave frequencies. However there is currently a need for higher accuracy between 18 and 35 GHz.

During the more than 45 years since the Becker and Autler measurements there have been numerous advances in microwave and environmental control technology. It therefore seems appropriate to reexamine the feasibility of conducting laboratory measurements to improve water vapor absorption coefficient accuracies.

This study begins with an examination of current requirements for atmospheric absorption coefficient accuracy. A discussion of theoretical issues pertaining to modeling atmospheric absorption and refraction spectra follows. Measurement strategies for improving coefficient accuracy including absorption cells, Fabry-Perot resonators, and single- and multimode cavity resonators are analyzed. Related measurement issues such as control and monitoring of the atmospheric sample are then reviewed. Finally, a detailed measurement strategy will be recommended for improving absorption coefficient accuracy.

II. Accuracy Requirements

The DSN need for accurate calibration of tropospheric path delays provides motivation for improving water vapor and dry air absorption coefficient accuracy. Tracing the connection between absorption measurements and DSN requirements allows coefficient accuracy to be estimated. Currently, requirements and goals for DSN determinations of atmospheric water vapor-induced propagation delays have been specified for the Cassini gravity wave search. This section will translate the existing requirements for calibration of water vapor-induced propagation delays into requirements on absorption coefficient accuracy.

A search for gravity waves will utilize measurements of the Doppler shift, Δf, induced in radio signals propagating between the earth and the Cassini planetary spacecraft [5]. Gravity waves will be manifested as perturbations in the observed spacecraft velocity, u_s. The spacecraft velocity is related to the one-way Doppler shift by

$$y = \frac{\Delta f}{f_o} = \frac{u_s}{c} = \frac{1}{c}\frac{dx_s}{dt} \qquad \textbf{(1)}$$

where f_o is the signal carrier frequency, x_s is the spacecraft position, and c is the speed of light. The sensitivity of the gravity wave search is expressed as an Allan variance, σ_y^2, of the observed fractional change in carrier frequency, y. Requirements for calibrating the troposphere set forth in the Cassini Ka-Band Radio Science Study are:

> "Measure atmospheric water vapor and temperature with sufficient accuracy to calibrate the lower atmospheric delay variations along the antenna boresight with an Allan deviation, $\sigma_y = 1.6 \times 10^{-15}$ for periods, τ, of 1,000 to 10,000 seconds and relaxing the Allan deviation as the inverse square root of the period, $\tau^{-1/2}$, from 1,000 to 100 seconds." [6]

The Cassini gravity wave search has also specified goals that are four times more stringent than the requirements [6]. These requirements apply to elevations angles ranging from 20° to zenith.

Transformation from the Allan deviation requirements to their corresponding power spectral density requirements starts with a conversion from Allan variance in fractional frequency to path delay. The relationship between power spectral density and Allan variance is

$$\sigma_y^2(\tau) = 4 \int_0^\infty \frac{S_y(f)\ \sin^4(\pi f\tau)}{(\pi f\tau)^2} df \quad , \tag{2}$$

where σ_y^2 is the Allan variance, τ is the integration or sampling time, and $S_y(f)$ is the two-sided fractional frequency power spectral density [5]. This transformation requires numerical integration and can be approximated with the following function (J. Armstrong, pers. comm.)

$$S_y(f) = \frac{9\times10^{-31}}{f} + 1.25\times10^{-27}\ (\mathrm{Hz}^{-1}) \quad . \tag{3}$$

Using the Fourier transform derivative theorem, the relationship between fractional frequency power spectral density, $S_y(f)$, and the path length power spectral density, $S_x(f)$, can be derived

$$S_x(f) = \frac{c^2}{8\pi^2 f^2}\ S_y(f) \quad . \tag{4}$$

This expression assumes the measurement of a two-way Doppler shift, which doubles the one-way Doppler spectral power. Finally the variance in path length is equal to the power spectral density integrated over the range of frequencies

$$\sigma_x^2 = 2 \int_{f_{low}}^{f_{high}} S_x\ (f)\ df = \frac{2c^2}{8\pi^2} \int_{f_{low}}^{f_{high}} \frac{S_y\ (f)\ df}{f^2} \simeq \frac{1.0\times10^{-11}}{f_{low}^2} + \frac{2.8\times10^{-8}}{f_{low}}\ \mathrm{cm}^2 \quad , \tag{5}$$

where f_{low} is the variance frequency of interest. This expression is dominated by the long period limit allowing the high frequency limit to be neglected. Substituting numbers into this formula is eye opening. The Cassini requirements translate into path delay errors, σ_y, of 400 μm over 10,000 second, 62 μm over 1000 seconds, and 17 μm over 100 second integration periods! The Cassini requirements for Doppler measurements are more stringent than the general Doppler goals, therefore the Cassini requirements will drive absorption coefficient accuracy.

The gravity wave search requirements are sensitive to the uncertainty in path delay variations and will be performed in the winter months when the zenith path delay may only average 1-2 centimeters. (Refining this assumption requires a database of path delay statistics that haven't been compiled for Goldstone.) At 10,000 seconds, the magnitude of the change in path delay will be dominated by the change in spacecraft elevation angle. When a satellite is tracked for 10,000 seconds from a worst-case 20° to 60° elevation angle, assuming 2 cm of zenith path delay, the path length change along the spacecraft line-of-sight will be 3.5 cm. At 10,000 seconds, the 400 μm accuracy requirement translates into 1.1% absorption coefficient accuracy. For integration times of 100 seconds, corresponding to a maximum 0.42° elevation angle change, movement from 20.00° to 20.42° provides only 1.1 mm path length change which is consistent with estimates of the magnitude of path delay changes due to vapor fluctuations. Assuming 1.1 mm change in the

total delay requires an absorption coefficient accuracy of 1.5% to achieve 17 μm accuracy (assuming that the path length variation is due solely to change in elevation angle).

Finally, water vapor emissions need to be corrected for radio noise emitted by molecular oxygen. An inaccurate correction will cause oxygen emissions to be attributed to water vapor causing an elevation angle-dependent offset in the water vapor retrieval. Absolute calibration requirements of 1 mm path delay accuracy and 17-400 μm path delay variance can be used to estimate the required accuracy of the oxygen absorption coefficients. A two-frequency WVR retrieval algorithm relating path delay to microwave sky brightness tailored for Goldstone [7] is:

$$\Delta L = 5.20 + 0.4946\ [T_B(20.7\ \text{GHz}) - 14.97] + 0.1547\ [T_B(31.4\ \text{GHz}) - 12.18]\ \text{cm}, \quad (6)$$

with ΔL representing water vapor induced path delay and $T_B(f)$ as brightness temperature expressed in kelvin (K). The 20.7 GHz brightness temperature is roughly 2.4 times the brightness temperature at 31.4 GHz [8]. This algorithm reveals that 1 cm of path delay corresponds to roughly 2 K at 20.7 GHz and 0.8 K at 31.4 GHz. Therefore 1 mm path delay error corresponds to 0.2 K and 0.08 K accuracy. To roughly estimate the brightness of oxygen, the water vapor-induced path delay can be set to zero, $\Delta L = 0$, corresponding to the case of no water vapor. Subtracting a cosmic background temperature of 2.74 K and assuming oxygen's sky brightness has a frequency-squared behavior yields an approximate zenith dry atmosphere brightness of 2.7 K at 20.7 GHz and 6.3 K at 31.4 GHz. Therefore 1 mm accuracy mapped to the sky brightness at 10° elevation angle corresponds to 1.3% oxygen absorption coefficient accuracy at 20.7 GHz and 1.8% accuracy at 31.4 GHz. For the 10,000 second gravity wave experiment requirement, 400 μm accuracy in the path delay variance using a measurement spanning from 20° to 60° elevation would impose 1.7% oxygen absorption coefficient accuracy at 20.7 GHz and 2.4% accuracy at 31.4 GHz. At 100 seconds using an elevation angle change from 20.00° to 20.42°, calibration requires 2.2% coefficient accuracy at 20.7 GHz and 3.0% at 31.4 GHz to achieve 17 μm path delay accuracy.

In conclusion, better than 0.8-1.0% absorption coefficient accuracy will be required to prevent absorption coefficient uncertainty from dominating the Cassini gravity wave search error budget for WVR determinations of water vapor-induced path delays. The current Cassini gravity wave *goals* require better than 0.5% accuracy.

III. Microwave Absorption Spectrum

A. Overview

A clear-sky tropospheric absorption/emission model spanning 15 to 40 GHz (Figures 1 and 3) can be separated into three distinct elements: the 22 GHz water vapor line, the low-frequency wing of the 60 GHz oxygen band, and the water vapor continuum. These three elements each have their own frequency-dependent sensitivity to meteorology (i.e., pressure, temperature, and humidity). Uncertainties in these dependencies exist for many of the components making up each element, especially dependence on temperature. Unfortunately, theoretical treatments of strong

molecular collisions are currently inadequate to independently determine appropriate parameterizations. However, general formulas have been developed which are based on both previous experimental measurements and theoretical arguments. These formulas can serve as *a priori* assumptions with which to interpret spectrometer data.

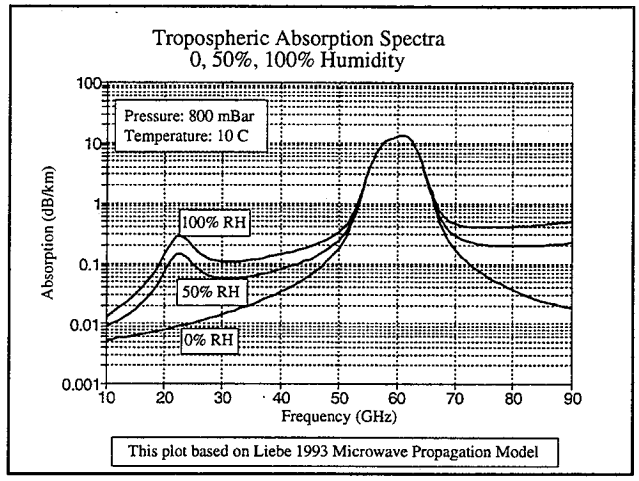

Figure 3. *Tropospheric Absorption Spectra*

The 22 GHz water vapor line and 60 GHz oxygen band result from different processes. The 22.23515 GHz spectral line is the lowest frequency resonance in the water vapor spectrum (neglecting isotopic resonant transitions) and results from a pure rotational transition between the $J = 6$, $K_{-1} = 1$, $K_1 = 6$ state located 447.30 cm^{-1} above ground state and the $J = 5$, $K_{-1} = 2$, $K_1 = 3$ state located at 446.56 cm^{-1} [9]. In contrast, the 60 GHz oxygen band results from transitions between the hyperfine split ground state levels [10] and consists of 43 overlapping lines [11]. The $^3\Sigma$ oxygen ground state is split because it is paramagnetic allowing dipole transitions between its magnetically separated levels [12]. Although magnetic dipole radiative transitions tend to be a couple orders of magnitude weaker than electric dipole induced transitions, the 60 GHz band remains a prominent spectral feature because of oxygen's abundance in the atmosphere.

B. 22 GHz Water Vapor Line

Collisionally broadened line shapes most frequently used to model the 22 GHz tropospheric water vapor line are the Gross [13], Van Vleck-Weisskopf [14], and Lorentzian [14] line shapes. Using a molecular-oscillator analog, the Lorentzian line shape assumes a random post-collisional distribution of oscillator phases, while the Van Vleck-Weisskopf line shape assumes that post-collisional phases are oriented preferentially with the electromagnetic wave's electric field. The Gross line shape assumes that post-collisional momenta are randomized leaving molecular oscillator phases undisturbed [13]. The appropriate line shape for calculational models has not yet been definitively determined, but available evidence favors use of the Van Vleck-Weisskopf shape with an empirical correction for the continuum [15]. Since deviations are expected from the Van Vleck-Weisskopf line shape at the percent level [16], it is recommended that Ben-Reuven's generalized line shape formalism [17, 18] be adopted for the water vapor line model. Ben-Reuven's line shape expression can be used to generate all three candidate line shapes.

The Ben-Reuven generalized line shape [17, 18] was developed to treat isolated and overlapping collision-broadened lines with pressures ranging from those found at mesospheric altitudes to several times that found at sea level. To formulate his shape function, Ben-Reuven used ω_o to represent the resonance frequency, with ω as the observation frequency, δ as the frequency shift parameter, and γ and ζ are two damping factors [19]. The frequency shift parameter, δ, is simply

a collision-induced shift in center frequency. The first damping factor, γ, is the linewidth parameter, and the other damping factor, ζ, is termed the coupling element. The linewidth parameter, γ, is proportional to the rate of collision resulting in a discontinuous change in oscillator phase. The coupling element, ζ, is correlated to the rate of collisions causing a phase rate sign change or a change in direction of molecular oscillator momenta. The classical oscillator analog models this coupling element, ζ, as a velocity-dependent frictional force. After a molecular collision, this element does not alter the oscillator phase, but rather reverses the direction of phase change. Ben-Reuven's shape factor can be written as $F(\omega)=F'(\omega)+iF''(\omega)$, [17, 18]

$$F'(\omega) = \frac{2\omega[\omega^2 - (\omega_0+\delta)^2 + (\gamma+\zeta)^2]}{[\omega^2 - (\omega_0+\delta)^2 - \gamma^2 + \zeta^2]^2 + 4\omega^2\gamma^2} \quad , \tag{7}$$

and

$$F''(\omega) = \frac{2(\gamma-\zeta)\omega^2 + 2(\gamma+\zeta)[(\omega_0+\delta)^2 + \gamma^2 - \zeta^2]}{[\omega^2 - (\omega_0+\delta)^2 - \gamma^2 + \zeta^2]^2 + 4\omega^2\gamma^2} \quad . \tag{8}$$

Applicability of the ζ coupling term to collisional broadening is limited to a specific class of systems where collisions can reverse the oscillator momentum. Ben-Reuven [18] gives the inversion spectrum of ammonia where collisions couple the two inversion states as an example of a system requiring the ζ coupling constant. Other examples cited are also characterized by closely spaced or overlapping spectral lines.

The Van Vleck-Weisskopf line shape can be derived by calculating the resonant case of Ben-Reuven's expression where there is neither a frequency shift nor momenta-reversing damping ($\delta=0$, $\zeta=0$),

$$F''(\omega) = \frac{\gamma}{(\omega-\omega_0)^2 + \gamma^2} + \frac{\gamma}{(\omega+\omega_0)^2 + \gamma^2} \quad . \tag{9}$$

The line strength, S, can modeled using the general form suggested by Liebe and Layton [20],

$$S = \frac{A_1}{T^{x_1}} \exp\left(A_2\left(1-\frac{A_3}{T}\right)\right) \tag{10}$$

where A_i are constants, T is absolute temperature, and x_1 is the temperature dependence radix (Liebe and Layton use $x_1 = 3.5$). Similarly the line width parameter can be modeled with

$$\gamma = \frac{A_4 P}{T^{x_2}} + \frac{A_5 e}{T^{x_3}} \tag{11}$$

where P is total pressure, e is the partial pressure of water vapor, and Liebe and Layton use their fits of $x_2 = 0.6$ and $x_3 = 1.1$ [20]. Since the Van Vleck-Weisskopf line shape has zero frequency shift and coupling constant, these parameters will initially be assumed to be small.

C. Oxygen Absorption

Molecular oxygen represents 21% of the atmosphere and contributes significant absorption between 15 and 40 GHz. The majority of this absorption is due to the 60 GHz oxygen band consisting of 43 overlapping lines. The remaining absorption is usually modeled as a weak non-resonant continuum due to Debye relaxation. This corresponds to the zero-frequency absorption term. Oxygen absorption has been modeled by Liebe, Rosenkranz, and Hufford based on their measurements between 49 and 67 GHz [21]. Because the use of measurements between 18 and 35 GHz only spans the low-frequency wing of the oxygen band, determining all 43 line parameters is impossible. Therefore, dry air absorption measurements will need to be fit to a simple polynomial approximating the more complete model. Then comparisons will be made between the polynomial fit and the complete Liebe et al. model.

D. Water Vapor Continuum

The water vapor continuum model is necessary because theoretical calculations of tropospheric water vapor absorption in the window regions significantly underestimate laboratory measurements. For example, in the 30 to 38 GHz window region, the candidate line shapes underestimate experimental measurements by 15 to 50%. Therefore a continuum correction represents a significant fraction of the total absorption. The worst case occurs under cool meteorological conditions, when various continuum models comprise more than 50% of the total vapor absorption [15].

Continuum absorption has several distinct traits: it spans wavelengths from the microwave (~5 cm) to the infrared (~10 μm), it appears to vary as frequency squared, it decreases rapidly with increasing temperature, and the magnitude of continuum absorption is greater in pure H_2O vapor than in an equivalent neutral-H_2O mixture (such as O_2-H_2O or N_2-H_2O) [22]. Several explanations have been suggested for the excess absorption. The two leading theories are that it is an artifact of an error in the far wing line shape of the submillimeter and infrared absorption lines [23, 24, 25, 26]; and that it is produced by water clusters, especially dimer transitions [27, 28, 29, 30]. Recently, a new calculational approach has reformulated the perturber-emitter collision model into a model that calculates the probability of two molecules emitting a single photon [31, 32]. This theory potentially combines both physical mechanisms. The dimer can be considered a case of two-molecule behavior over long durations. Similarly, the far wing line shape would be a case of interaction between two molecules over much shorter periods. The multimolecule framework has been used to calculate continuum absorption and gives rough agreement with observational data.

In order to model continuum absorption over the limited range of 15 to 40 GHz, the general Liebe and Layton formalism will be adopted [20]. Their expression has two terms: The first term corresponds to contributions from water vapor interacting with "foreign" molecules such as nitrogen and oxygen; and the second term describes the "self-broadening" contributions (water vapor-water vapor interactions). Water vapor molecules are capable of stronger interaction forces than other atmospheric gases because water vapor is strongly polar, while the others are nonpolar. Since there are many more foreign gas collisions in the atmosphere due to the abundance of nitrogen and oxygen, the two terms have similar magnitudes. The general two-term expression for the continuum is

$$\alpha(\nu) = \nu^2 \left(\frac{B_f\, eP}{T^{x_f}} + \frac{B_s\, e^2}{T^{x_s}}\right) \qquad (12)$$

where ν is the observation frequency, B_i are constants, T is temperature, x_i are the temperature power-law radices, e is the partial pressure of water vapor, and P is the total gas pressure.

The total absorption spectral model can now be constructed by summing the three model elements

$$\alpha(\nu,a,T,P,e) = S(T,e,P)F''(\nu,\gamma)_{vapor} + \alpha(\nu,T,P,e)_{continuum} + S(T,e,P)F''(\nu,\gamma)_{O_2} \quad . \qquad (13)$$

E. Atmospheric Refractivity

Atmospheric microwave refractivity, N, can be written [33],

$$N = K_1\frac{P}{T}Z_a^{-1} + K_2\frac{e}{T}Z_w^{-1} + K_3\frac{e}{T^2}Z_w^{-1} \quad , \qquad (14)$$

where e is the partial pressure of water vapor, P is the partial pressure of dry air (i.e., N_2, O_2, CO_2), T is the absolute temperature, K_i are constants which combine all of the other material-dependent parameters into one number, and Z_i^{-1} are the compressibility factors from Owens [34] that account for deviations between behavior of real atmospheric gases and "ideal" gas law gases. The nonpolar gases comprising dry air have a density (P/T) dependence; water vapor, which is polar, has both a density (e/T) and a density/temperature (e/T^2) dependent term [35]. The last density/temperature-dependent term represents roughly 94% of total water vapor refractivity. Theoretical predictions of water vapor refractive temperature dependence differ slightly from this expression. However, use of this formulation will only incur 0.03% rms error [33].

The material dependent constants (K_i) have been determined using cavity refractometer measurements. The most recent determinations of K_1 have yielded a value of 776.0 K/kPa with an experimental error of less than 0.1% [36, 37]. The most recent experimental determinations of water vapor refractivity were those made by Boudouris [37]. His values for the refractive constants are $K_2 = 720 \pm 100$ K/kPa and $K_3 = (3.754 \pm 0.03) \times 10^6$ K^2/kPa which were measured with an accuracy of 1.3%. The errors stated for K_2 and K_3 represent the uncertainty in the fit used

to separate K_2 from K_3. Many other researchers have measured the refractivity of water vapor and these values are reviewed in Boudouris [37], Bean and Dutton [38], and Walter [39]. It has been suggested that averaging measurements made by several investigators can provide an independent assessment of the accuracy of Boudouris' error figure. Unfortunately, the choice of experiments which should be used and what weights should be assigned in averaging them is not clear. For example, there are legitimate questions of whether measurements made on steam are applicable to atmospheric conditions or whether certain researchers were able to correct for vapor condensation on the walls of their sample cells. Although construction of a credible average is beyond the scope of this study, a conservative estimate of the agreement between Boudouris' determinations [37] and those of other researchers is 1%.

The need to add a frequency-dependent correction to the expression for refractivity is minimal. Below 40 GHz, the magnitude of refractive dispersion in Liebe and Layton's model [20] is less than 0.035%. Their dispersion model is based on Liebe and Gimmestad's measurements [40].

F. Conclusion

Recommendations for the initial model to be used to interpret cavity spectral data can be summarized as follows. In the case of oxygen, a polynomial fit should be used to model dry air measurements. The resulting fit can then be validated against the Liebe, Rosenkranz, and Hufford model [21]. Since all of the line shapes currently used to model the 22 GHz water vapor resonance can be derived from the Ben-Reuven's generalized line shape formulation, water vapor measurements can be used to calibrate parameters in Ben-Reuven's model [17, 18]. Additional line shape parameters such as line strength and line width should use Liebe and Layton's expression [20]. The water vapor continuum model should have both a self-broadening and foreign-gas broadening term also patterned after Liebe and Layton [20]. Finally, the tropospheric refractive spectrum is essentially nondispersive and therefore will not require a dispersion model.

IV. Microwave Spectroscopy

A. Introduction

The microwave characteristics of a gas can be determined with absorption cell or cavity resonator spectrometers. Absorption cell spectrometers directly measure absorption induced by a gas sample in a calibrated propagation path. Cavity spectrometers infer absorption from the change in the quality factor referred to as the "Q" which is related to the resonance bandwidth. Therefore making frequency measurements on a gas-filled resonator can determine absorptivity. Resonators can also determine the refractive index without much additional effort because the refractive index can be calculated from the shift in a cavity's resonance frequency.

Atmospheric water vapor is both a weak absorber and emitter (between 18 and 40 GHz). While this gains the advantage of minimizing radiative corrections needed in passive remote sensing, it also significantly increases the difficulty in laboratory measurements. As was shown in figures 1 and 3, atmospheric absorptivity between 15 and 40 GHz ranges from roughly 0.01

dB/km to 0.5 dB/km. Over laboratory distances of 1 to 2 meters, this translates to attenuations of less than 10^{-3} dB. Measuring these attenuations with better than 1% accuracy requires measurement accuracies of 10^{-4} to 10^{-7} dB. This section will investigate how absorption cells, Fabry-Perot resonators, and single- and multimode cavity resonators can be used to make spectroscopic measurements of weakly absorbing gases.

B. Absorption Cells

A basic single-pass microwave absorption spectrometer consists of a source which transmits a signal through a cell containing a gas sample to a detector. The change in signal strength caused by introduction of the gas sample can be used to calculate absorption. In the case of a single-pass cell, the absorption coefficient is simply

$$\alpha = \frac{\Delta P}{L} \tag{15}$$

where α is the absorption coefficient, ΔP is the change in transmitted power (expressed in decibels) induced by the gas sample, and L is the sample cell length. In the single-pass cell, absorption is derived from the difference between two power measurements. For a weakly absorbing gas this technique requires very accurate power measurements because the source and detected power levels will be comparable yielding a very small difference signal. Under ideal conditions, state-of-the-art measuring receivers and network analyzers can achieve accuracies of roughly 0.02 dB for signal strengths which are similar to the source strength [41, 42]. Therefore, simply to observe water vapor-induced attenuation (~0.5 dB/km) requires a sample cell that is in excess of 40 meters long. To measure the absorption with 1% accuracy requires a sample cell that is 100 times longer. Use of a single-pass absorption cell spectrometer is clearly impractical for measuring weakly absorbing gases.

Double-pass absorption cell spectrometers are much more sensitive to small absorptivities. A double-pass absorption cell passes the source signal through a gas cell to a mirror which reflects the transmitted signal back toward the source, generating a standing wave pattern. Located between the source and sample cell is a test section with probes that measure the standing wave pattern. This section usually consists of a slotted line and coupling probe. Assuming lossless waveguides, test section, and sample cell, as well as a perfect mirror and a weakly absorbing gas, the difference in the standing wave peak and null amplitudes can be used to determine absorptivity. In this case, absorption is

$$\alpha = \frac{10}{L} \log_{10}\left(\frac{10^{\Delta P/20}+1}{10^{\Delta P/20}-1}\right) \approx \frac{20 \log_{10} e}{L} 10^{-\Delta P/20} \quad for\ \Delta P \geq \sim 20\ dB \tag{16}$$

where L is the length of the cell and $\Delta P = P_{peak} - P_{null}$ is the difference in power (expressed in dB) at the peaks and nulls of the standing wave pattern. For a weakly absorbing gas, the double-pass cell technique differs from that of a single-pass cell because the interference that generates the standing wave essentially performs the power difference calculation. This lessens the

requirements on the accuracy of each power measurement, but also introduces stringent requirements on source stability.

A simulation was run to assess the measurement accuracy obtainable with a double-pass cell. To achieve 1% accuracy requires measurement of the peak-to-null power difference that is slightly better than 0.09 dB. Unfortunately, this technique is limited by the large size of the peak-to-null power differences. For a one-meter cell, the difference in power will range from 85 to 110 dB (corresponding to a range of 0.5 to 0.03 dB/km). Lengthening the cell to ten meters will not affect the required measurement accuracy, but will reduce the range of peak-to-null power differences to between 65 to 90 dB. Electromagnetic interference (EMF), crosstalk, scattering, and the finite size of the power sensors will prevent power differences of these magnitudes from being accurately measured.

C. Cavity Resonators

A simple resonator-based spectrometer consists of a signal source coupled to a resonator whose amplitude response is monitored by an external detector. At microwave frequencies hollow conducting cavities are commonly used as resonators. Electromagnetic energy confined within a cavity reflects from wall to wall, interfering with itself to create a three-dimensional standing wave pattern. It eventually dissipates through resistive losses in the cavity walls, absorption by the cavity contents, and leakage through cavity apertures such as signal ports. The shift induced in a cavity's resonant frequency by an internal gas sample can be used to calculate the refractivity of the gas. Similarly, absorptivity of the gas can be calculated from the change it induces in a resonator's capacity to store energy.

Applying Maxwell's equations (or the wave equation) with appropriate boundary conditions yields the field distribution inside a resonant structure. The resulting energy distribution can be decomposed into an orthogonal set of modes, called eigenmodes, that are dictated by the cavity geometry. For example, eigenmodes in a rectangular cavity are best described by trigonometric functions, while the radial components of a cylindrical cavity naturally decompose into Bessel functions. These decompositions are physically significant because each eigenmode corresponds to a characteristic frequency called an eigenfrequency, or resonance frequency.

A cavity's eigenfrequency is sensitive to the contained medium or "load," so the refractivity of a gas can be derived from the shift it induces in the eigenfrequency. As a gas sample is introduced into a previously evacuated cavity the propagation speed decreases, making the cavity look effectively larger, decreasing the eigenfrequency f_c. The refractive index n of a gas inside a cavity can be calculated as a ratio of the evacuated eigenfrequency f_{cv} to the loaded eigenfrequency f_{cl} ,

$$n = \frac{f_{cv}}{f_{cl}} \quad . \tag{17}$$

If necessary the vacuum eigenfrequency can be extrapolated from frequencies measured over a range of pressures of a nondispersive gas.

Energy storage capacity in a cavity is also sensitive to the properties of internal medium, thus providing a means for measuring absorptivity. The dimensionless parameter Q, called the "quality factor," is a useful quantity relating a resonator's energy storage capacity to its dissipation rate,

$$Q = \omega \frac{U}{W_L} \quad , \tag{18}$$

where $\omega = 2\pi f$ is the angular frequency, U is the average energy stored in the resonator's fields, and W_L is the energy loss rate from all sources. W_L is given by

$$W_L = W_w + W_r + W_a \quad , \tag{19}$$

where W_w is the loss rate due to cavity wall resistivity, W_r is the total radiative loss rate (i.e., leakage through cavity apertures), and W_a is the loss rate due to absorption by the cavity contents. Q is intrinsic to a resonator's geometry and implementation, independent of field strength; so for a given resonator, it is primarily determined by the cavity shape and wall resistivity. At a given frequency Q increases with cavity volume and decreases with surface area and wall resistivity. Notably, Q decreases with absorptivity α of the cavity's internal medium, because an increase in α increases W_a and thus W_L. Quantifying this relation leads to the techniques for measuring α with resonators.

The energy density ρ_E in an electromagnetic field is given by

$$\rho_E = \frac{1}{2} (E \cdot D + B \cdot H) \quad , \tag{20}$$

where **E** and **D** are the electric and displacement fields ($\varepsilon\mathbf{E} = \mathbf{D}$) and **B** and **H** are the magnetic induction and magnetic field ($\mathbf{B} = \mu\mathbf{H}$) [43]. Total energy can be determined by integrating the energy density over the volume of interest. A simple trick aids in this calculation. For a system where the electromagnetic energy density is constant, the total energy will oscillate between magnetic and electric energy. At the moment the electric field is at a maximum, the magnetic field will be zero and vice versa. Computing the energy at the maximum electric field strength eliminates the need for the magnetic field energy term [44]. Using a rectangular cavity of dimensions $a \times b \times d$ as an example, [44]

$$U = U_{E_{\max}} = \frac{\epsilon}{2} \int_0^d \int_0^b \int_0^a |E_{\max}|^2 \, dx \, dy \, dz \quad . \tag{21}$$

This expression shows that the total energy in each cavity mode is proportional to the cavity volume times the square of its maximum electric field strength.

In an unloaded, weakly coupled cavity, energy is dissipated primarily by wall currents induced by tangential magnetic fields. Power dissipation by wall losses can be calculated by integrating

the product of the square of tangential magnetic field strength and wall's surface resistivity over the cavity's total surface area [44]. Again using the rectangular cavity as an example, this can be expressed as

$$W_L = \frac{R_s}{2} \sum_{i,j,k} \left(2 \int_0^{l_j} \int_0^{l_i} |H_i|^2_{k=0} \, dx_i \, dx_j \right) \quad , \tag{22}$$

where R_s is the surface resistivity of the cavity walls, H_i is the magnetic field in the i^{th} direction, and i, j, and k are the three indices corresponding to the three x_i, the orthogonal coordinates [44]. This expression shows that wall dissipation is proportional to the total wall area times its material surface resistivity and the tangential magnetic field strength squared for the given mode.

The equation defining the quality factor can be inverted to yield

$$\frac{1}{Q} = \frac{1}{\omega U}(W_w + W_r + W_a) = \frac{1}{Q_c} + \frac{1}{Q_r} + \frac{1}{Q_g} \tag{23}$$

where Q_c is the cavity Q, Q_r quantifies radiative losses (that reduce Q) through various apertures, and Q_g is associated with the load (i.e., the internal medium). In the general case,

$$Q_c = A \frac{\eta}{R_s} G(a,b,d) \quad , \tag{24}$$

where A is a constant, η is the internal medium intrinsic impedance, R_S is the cavity wall surface resistivity, and $G(a,b,d)$ is a geometrical factor that depends on cavity geometry. At a fixed frequency Q_c is constant. This is also true of Q_r, since both U and W_r are proportional to the square of the field strengths. Measurement of a resonator's Q under loaded conditions and unloaded conditions (no absorptive losses, so $1/Q_g = 0$) yields Q_l and Q_u respectively. The Q of the absorptive medium, Q_g, can be inferred from those quantities,

$$\frac{1}{Q_g} = \frac{1}{Q_l} - \frac{1}{Q_u} \quad . \tag{25}$$

This is true if the mode frequency for unloaded measurements is identical to that of loaded measurements, requiring that the refractive index of the cavity's contents be identical in both cases. This is necessary because the cavity wall resistivity, R_s, is proportional to the square root of frequency [44]; hence both Q_c and Q_r are functions of frequency. So even when a lossless gas is introduced into the cavity, the observed Q is different from the vacuum value. This phenomenon, called "dielectric loading," is a combination of various phenomena related to frequency changes and leakage [45], and must be addressed by the measurement strategy.

It might be possible to calculate the relationship between cavity Q and the refractive index for a lossless medium; then the Q_u could be calculated from Q_v, (the vacuum Q). However, accurate calculations are difficult and can be a significant source of systematic errors. An alternate method

is to measure Q_u with a lossless gas such as nitrogen at a pressure which allows its refractive index to match that of the loaded cavity [45]. In other words, the nitrogen pressure is adjusted until the cavity eigenfrequency is identical to that of the loaded cavity.

When Q_g is known, the absorptivity α of the gas can be related to Q_g by [44]

$$\alpha = \frac{\pi f_{cl}}{v}\left(\frac{1}{Q_g}\right) , \tag{26}$$

where f_{cl} is the mode's frequency under loaded conditions, v is propagation speed in the medium, and α is in nepers per unit length. The Q_g of water vapor at 22 GHz for 0.4 dB/km of absorption is roughly 6×10^6. An absorptivity of 0.08 dB/km at 30 GHz yields a Q_g of 40×10^6. Substituting Q_g, as defined in Equation 24 and using $c = nv$, generates an expression in terms of Q_l and Q_u,

$$\alpha = \frac{\pi n f_{cl}}{c}\left(\frac{1}{Q_l} - \frac{1}{Q_u}\right) . \tag{27}$$

Multiplying by 20 $\log_{10}e$ (~8.686) converts α to units of dB per unit length. Unfortunately, Q values cannot be measured directly, but must be determined from properties of the cavity resonance that can be measured.

Q can be calculated from a resonator's center frequency, ω_o, and rate of energy dissipation. Rewriting the expression for power dissipation, W_L, as the rate of energy loss, $-dU/dt$, generates a differential equation for energy dissipation [46]

$$\frac{dU}{dt} = -\frac{\omega_o}{Q}U . \tag{28}$$

The solution has the form,

$$U(t) = U_o e^{-\frac{\omega_o t}{Q}} , \tag{29}$$

where U_o is energy stored in the cavity at time $t = 0$ [46]. This illustrates that Q is directly related to the characteristic decay time for energy stored in a cavity. Therefore, an increase in Q will cause an increase in energy dissipation time. This damping dependence implies a similar dependence for the field strength whose decay must take the form

$$E(t) = E_o\, e^{-\omega_o t/2Q}\, e^{-i(\omega_o+\Delta\omega)t} , \tag{30}$$

where E_o is the initial field strength, $\Delta\omega$ is the shift in center frequency introduced by damping, and t is time [46]. The Fourier transform of the electric field yields a Lorentzian line shape,

$$|E(\omega)|^2 \propto \frac{1}{(\omega-\omega_o-\Delta\omega)^2 + (\omega_o / 2Q)^2} , \tag{31}$$

using ω as the frequency of interest. The resonance full width, Γ, is simply frequency, ω_o, divided by Q. Thus Q determines a resonator's bandwidth,

$$\frac{1}{Q} = \frac{\Gamma}{\omega_o} \simeq \frac{\Delta f}{f_c} \tag{32}$$

where Δf is the cavity bandwidth and f_c is the eigenfrequency for a given cavity mode [46]. Both Δf and f_c can be directly measured with a spectrum analyzer. Now the absorptivity α can be rewritten as

$$\alpha = \frac{\pi n f_{cl}}{c}\left(\frac{\Delta f_{cl}}{f_{cl}} - \frac{\Delta f_{cu}}{f_{cu}}\right) \tag{33}$$

here the subscript *cl* refers to a cavity with an absorptive load and *cu* refers to a cavity with a lossless load. Since the refractive matching technique ensures that $f_{cl} = f_{cu}$,

$$\alpha = \frac{\pi n}{c}\left(\Delta f_{cl} - \Delta f_{cu}\right) \tag{34}$$

The increase in cavity bandwidth, Δf_{cl} - Δf_{cu}, induced by water vapor ranges from 5 kHz for 0.5 dB/km to 110 Hz for 0.01 dB/km. To determine absorptivity of the cavity load with the requisite accuracy will require measuring the cavity bandwidth to roughly 5 to 10 Hz. Increasing the unloaded cavity Q will improve the accuracy to which changes in Q induced by the internal medium can be resolved.

Another technique exploits the change in a mode's peak amplitude with changing Q. At a constant frequency and injected signal power, the peak field amplitude inside the cavity is a function of the internal medium's absorptivity [Spilker, in preparation],

$$E_l = E_u\left(1 + 2Q_u\frac{\alpha}{\beta}\right)^{-1/2} , \tag{35}$$

where E_l is peak electric field strength under loaded conditions, E_u is peak strength under unloaded conditions, and $\beta = 2\pi/\lambda$ is the internal medium "phase constant" at f_{cl} . As in the previous method, this technique requires refractive index matching for the unloaded resonator which ensures that β remains constant. The measured quantities, P_l and P_u, are power ratios of the detected power to the injected power for the loaded and unloaded cases, respectively. Since the peak signal power reaching the spectrum analyzer (or other detecting device) is proportional to the square of the peak field amplitude, power measurements can be substituted for the squared field strengths yielding

$$\alpha = \frac{\pi n f_{cl}}{c Q_{cu}}\left(\frac{P_u}{P_l} - 1\right) \tag{36}$$

where α is in nepers per unit length. Since $f_{cl} = f_{cv}$ and $Q \approx f_c/\Delta f$, this reduces to

$$\alpha = \frac{\pi n \Delta f_{cu}}{c} \left(\frac{P_u}{P_l} - 1 \right) \quad . \tag{37}$$

For weak absorbers this method can provide a rough check on the accuracy of the bandwidth measurements. Using a resonator with a Q of 10^6 to measure an absorptivity of 0.4 dB/km at 22 GHz, the power ratio, P_u/P_l, is 1.2; at 0.08 dB/km and 30 GHz the power ratio is only 1.03. The power ratios increase monotonically with cavity Q; the higher the Q of the unloaded cavity, the greater the accuracy to which the power ratio can be measured.

This study examines two general classes of resonators: rectangular cavities and Fabry-Perot resonators. Rectangular (or parallelepiped) cavities are considered because even large ones are relatively easy and inexpensive to fabricate. Fabry-Perot resonators, which consist of two parallel mirrors, yield high Q values for a given volume and have an open structure which simplifies environmental control. Since spectroscopic measurements can also be made using resonators that excite multiple modes, the feasibility of a multimode approach is investigated for a rectangular cavity geometry.

D. Rectangular Resonators

Electromagnetic fields inside a hollow conducting parallelepiped chamber can form three-dimensional standing wave patterns producing a regular spectrum of eigenmodes. The nulls in the field patterns are classified by the axes along which they are distributed. Each null defines a nodal plane which is perpendicular to a cavity axis (or alternatively, parallel to a set of opposing walls). Nodal planes partition the cavity interior into smaller parallelepipeds of equal size with antinodes at each of their centers. A given mode is designated by three integers which define the "mode order." Each number in a mode order specifies the number of antinodes along the axis it represents, with zero representing zero field components along that axis. Inside a resonator, the traveling waves that combine to produce the eigenmode standing wave pattern can be described by their wave vectors, $\bar{k}$'s, which are vector sums of their components along each of the cavity axes

$$\bar{k} = \bar{k}_x + \bar{k}_y + \bar{k}_z \quad . \tag{38}$$

The magnitude of $\bar{k} = \beta = 2\pi/\lambda$ is given by

$$k^2 = k_1^2 + k_2^2 + k_3^2 \quad , \tag{39}$$

where k_i are the magnitudes of the components oriented along the x, y, and z axes, respectively.

A rectangular cavity with dimensions $a \times b \times d$, corresponding to coordinate axes $[x,y,z]$, has mode orders $[n,m,l]$. Cavity modes are classified into two different classes: transverse electric ($TE_{n,m,l}$) modes where there is no net electric field oriented along one of the axes, and transverse magnetic

($TM_{n,m,l}$) modes where there is no net magnetic field oriented along one axis. Convention dictates that the z axis is the coordinate with zero field. Applying the rectangular boundary conditions to Maxwell's equations yields the general field equations for the eigenmodes. Since the analysis of rectangular conducting cavities appears in numerous texts such as [10], [44], [47], and [48], those derivations will not be repeated here. For the cavity described above, components k_i are related to the mode order and cavity dimensions by the formulas

$$k_1 = \frac{n\pi}{a} \qquad k_2 = \frac{m\pi}{b} \qquad k_3 = \frac{l\pi}{d} \quad . \tag{40}$$

The field equations for the $TE_{n,m,l}$ and $TM_{n,m,l}$ modes are, respectively, [48]:

$$\left.\begin{aligned}
E_x &= \frac{-k_2}{k} \cos k_1 x \sin k_2 y \sin k_3 z \quad , \\
E_y &= \frac{k_1}{k} \sin k_1 x \cos k_2 y \sin k_3 z \quad , \\
E_z &= 0 \quad , \\
H_x &= \frac{k_1 k_3}{k^2} \sin k_1 x \cos k_2 y \cos k_3 z \quad , \\
H_y &= \frac{k_2 k_3}{k^2} \cos k_1 x \sin k_2 y \cos k_3 z \quad , \\
H_z &= \frac{-k_1^2 - k_2^2}{k^2} \cos k_1 x \cos k_2 y \sin k_3 z .
\end{aligned}\right\} \quad \begin{array}{c} l > 0 \\ \textit{and} \\ n \textit{ or } m > 0 \end{array} \tag{41}$$

$$\left.\begin{aligned}
E_x &= \frac{k_1 k_3}{k^2} \cos k_1 x \sin k_2 y \sin k_3 z \quad , \\
E_y &= \frac{k_2 k_3}{k^2} \sin k_1 x \cos k_2 y \sin k_3 z \quad , \\
E_z &= \frac{-k_1^2 - k_2^2}{k^2} \sin k_1 x \sin k_2 y \cos k_3 z , \\
H_x &= \frac{-k_2}{k} \sin k_1 x \cos k_2 y \cos k_3 z \quad , \\
H_y &= \frac{k_1}{k} \cos k_1 x \sin k_2 y \cos k_3 z \quad , \\
H_z &= 0 \quad .
\end{aligned}\right\} \quad \begin{array}{c} n > 0 \\ \textit{and} \\ m > 0 \end{array} \tag{42}$$

The eigenfrequencies for a rectangular cavity are determined by mode order and cavity dimensions,

$$f_{n,m,l} = \frac{v}{2}\left(\left(\frac{l}{d}\right)^2 + \left(\frac{m}{b}\right)^2 + \left(\frac{n}{a}\right)^2 \right)^{1/2} \quad , \tag{43}$$

where v is the propagation velocity inside the resonator [47]. TE and TM modes with identical mode orders are "degenerate" (i.e., have the same eigenfrequency), so this equation is valid for both classes of eigenmodes. Energy stored in the cavity can be calculated using Eq. 21 [44]

$$U = \frac{\epsilon abd}{8} E_o^2 \quad , \tag{44}$$

where ε is the dielectric constant of the cavity's internal medium and E_o is the maximum electric field strength. This is a general expression that is valid for multiple modes and both types of eigenmodes. The lossless (unloaded) Q for the TE modes is given by

$$\frac{1}{Q} = \frac{\delta}{\lambda}\frac{4}{abd}\frac{ad(p^2r^2+(p^2+q^2)^2) + bd(q^2r^2+(p^2+q^2)^2) + ab(r^2(p^2+q^2))}{(p^2+q^2)(p^2+q^2+r^2)^{3/2}} + \frac{1}{Q_r} \quad . \tag{45}$$

where λ is the traveling wave wavelength in the internal medium, δ is the cavity wall skin depth, Q_r is caused by radiative losses, $p = n/a$, $q = m/b$, and $r = l/d$. This expression is valid for $n > 0$ and $m > 0$ [48]. For TM modes Q is simply

$$\frac{1}{Q} = \frac{\delta}{\lambda}\frac{4}{abd}\frac{p^2b(a+d) + q^2a(b+d)}{(p^2+q^2)(p^2+q^2+r^2)^{1/2}} + \frac{1}{Q_r} \quad . \tag{46}$$

Systematic errors occur when there are small perturbations in the size of the cavity. The change in eigenfrequency due to a change in a cavity dimension can be calculated from the partial derivative of the eigenfrequency equation with respect to one of its dimensions. For small changes in dimension, δa, the corresponding decrease in eigenfrequency is

$$\delta f_{n,m,l} = \frac{df_{n,m,l}}{da}\,\delta a \simeq \frac{-v^2}{4}\left(\frac{n}{a}\right)^2\left(\frac{1}{af_{n,m,l}}\right)\delta a \quad . \tag{47}$$

A proportional increase in all dimensions will induce an approximately linear increase in Q. For example, a one-meter cavity excited at 30 GHz and mode order $n = 115$, will change in resonant frequency with a dimensional change at a rate of approximately -10^{10} Hz/m. Therefore, to measure bandwidth to 5 Hz, the resonator cannot change dimension during the measurement by more than 0.5 nm! In general this dependence is a function of mode order and cavity dimensions, so it will be treated numerically when a specific design is being considered. Finally, the change

in Q caused by a change in cavity wall resistivity R_S can be derived using the relationship between the skin depth, δ, and conductivity σ ($\delta = \{R_s\sigma\}^{-1}$), yielding a simple linear relationship

$$\frac{dQ}{dR_s} \simeq \frac{Q}{R_s} \quad for\ Q \gg Q_r. \tag{48}$$

Therefore water condensation on cavity walls will change the Q by the same percentage that condensation changes the wall resistivity. This development provides the foundation for determining the suitability of a rectangular parallelepiped cavity for determining water vapor absorption coefficients in section IV.I.

E. Fabry-Perot Resonators

In the late 1950's Townes and Schawlow proposed that an open structure consisting of two parallel walls could eliminate an enormous number of modes present in a closed cavity [44]. They reasoned that modes whose energy did not reflect between the two walls would be damped when the energy exited the resonator. Analysis of this geometry was equivalent to work done by Charles Fabry and Alfred Perot, who developed a multiple beam interferometer incorporating two parallel mirrors [49] in the late 1800's. Electromagnetic waves launched into the cavity (the region between the two mirrors) are repeatedly reflected back and forth until a steady-state field distribution is reached [50]. As energy continues to be injected, the energy density continues to increase until equilibrium is reached with a combination of resistive losses in the mirrors, leakage through input and output apertures, diffraction around the mirror edges, and absorption by the medium between the mirrors (the "internal medium," or in the lossy case the "load"). A high-Q resonator consisting of parallel mirrors is often called a Fabry-Perot interferometer, a Fabry-Perot resonator, or an etalon [51].

Fabry-Perot configurations can be classified according to the shape and spacing of the mirrors. Use of plane-parallel mirrors provides a structure that is equivalent to the rectangular cavity where standing wave patterns are excited in only one direction. This roughly corresponds to the case where two of the mode numbers are zero. Using spherical mirrors defines a family of Fabry-Perot resonators classified by the ratio of the mirror curvature to the mirror spacing. Using identical concave mirrors can significantly reduce diffraction losses when the distance between mirrors is equal to the mirrors' radius of curvature [51]. This specific configuration is termed a confocal Fabry-Perot resonator [51]. Using one flat mirror and one concave mirror can have some benefits. The diffraction losses are minimized when the distance between the mirrors is half the spherical mirror's radius of curvature. This configuration is termed a semi-confocal Fabry-Perot resonator [20, 52]. The analysis in this section will concentrate on the confocal Fabry-Perot resonator geometry.

Spherical rather than parabolic mirrors are recommended for confocal resonators. Parabolic mirrors are expensive to fabricate and require very careful adjustments to align their optical axes,

while spherical mirrors are easier to fabricate and provide a better match to the near-spherical traveling wave phase fronts. Confocal mirror spacing yields the smallest beam radius or "spot size" at the mirrors, which minimizes the diffraction losses [49].

The spot size at the mirror (defined by e^{-1} reduction in power) for a confocal geometry is

$$w_s \simeq \sqrt{\frac{b\lambda}{\pi}} \quad , \tag{49}$$

where λ is the radiation wavelength and b is the spacing between the mirrors [49]. The mirror size is determined by calculating the radius, a, at which diffraction losses begins to diminish the resonator Q. This can be quantified with the Fresnel number, $N = a^2/\lambda b$. Diffraction losses tend to be negligible for Fresnel numbers much greater than unity [44].

Modes in a Fabry-Perot resonator are transverse electromagnetic modes, $TEM_{n,m,p}$ [49]. These modes have their electric and magnetic fields perpendicular to the propagation axis. Convention selects the propagation axis, which is the centerline between the mirrors, as the z axis. Mode order p corresponds to modes with nodes situated along the z axis. The eigenfrequencies for a confocal Fabry-Perot are

$$f_{n,m,p} = \left(\frac{v}{4b}\right)(1 + 2p + m + n) \quad , \tag{50}$$

with mode order $[n,m,p]$ and propagation speed v between the mirrors. Semi-confocal resonators will resonate at the same eigenfrequencies as confocal resonators [53]. For a resonator with a Fresnel number greater than 0.7 the Q is more than an order of magnitude greater for the fundamental $TEM_{0,0,p}$ modes, than the higher order $TEM_{n,0,p}$ modes (where $n \geq 1$) [49]. Therefore a high-Q Fabry-Perot cavity will normally resonate in a $TEM_{0,0,p}$ mode.

Taking the partial derivative of this equation with respect to b yields the change in an eigenfrequency due to a small change in the intermirror distance:

$$\frac{df_{n,m,p}}{db} = -\frac{f_{n,m,p}}{b} \quad . \tag{51}$$

The observed Q of the resonator can be related to the sum of four terms,

$$\frac{1}{Q} = \frac{1}{Q_D} + \frac{1}{Q_i} + \frac{1}{Q_r} + \frac{1}{Q_g} \quad , \tag{52}$$

representing losses from diffraction, mirror reflectivity, coupling apertures, and absorption by the internal medium, respectively. If perfectly shaped mirrors are assumed the diffractive term is given by

$$\frac{1}{Q_D} = \frac{\lambda}{2\pi b}\alpha_D \quad , \tag{53}$$

where α_D is the fractional power loss per reflection due to diffraction and $\lambda/2\pi b$ is an energy scaling factor. For large Fresnel number N, α_D can be approximated by

$$\alpha_D = 1 - |\sigma_n \sigma_m|^2 \simeq 16\pi^2 N e^{-4\pi N} \tag{54}$$

where σ_i's are eigenvalues of spheroidal wave functions [44]. Deviations from ideal mirror shape can add significantly to these losses. The radiation wavelength and the material properties of the mirrors and the internal medium determine the intrinsic quality term

$$\frac{1}{Q_i} = \frac{\lambda}{2\pi b}\alpha_i = \frac{\lambda}{2\pi b}\sqrt{\frac{\pi}{\eta \sigma \lambda}} \quad , \tag{55}$$

where α_i is the fractional power loss per reflection due to mirror surface resistivity, σ is the conductivity of the mirror material and η is the intrinsic impedance of the internal medium. Q_r is determined by the geometry of the input and output apertures. It can be expressed in terms of the energy scaling factor

$$\frac{1}{Q_r} = \frac{\lambda}{2\pi b}\alpha_r \quad , \tag{56}$$

where α_r is the fractional power loss per reflection due to coupling energy out through the apertures. Q_r can easily dominate cavity losses, so aperture design is critical. Finally, Q_g is the quality factor of the internal gaseous medium as defined in section IV.C.

Combining these terms, the observed Q can be expressed by

$$\frac{1}{Q} = \frac{\lambda}{2\pi b}(\alpha_D + \alpha_i + \alpha_r) + \frac{1}{Q_g} \quad . \tag{57}$$

This formulation emphasizes the fact that Q_D, Q_i, and Q_r are constant for a fixed radiation frequency and internal medium refractivity. Hence, it shows that the cavity resonator's refractive matching technique for isolating Q_g can also be used with a Fabry-Perot resonator. The absorptivity reduction equation for the Fabry-Perot is also identical to that for the cavity resonator.

Boyd and Gordon [49] calculated the total Q for a confocal resonator and found the diffraction loss is an eighth of the reflection loss for a Fresnel number N of 0.8. Therefore in order to make the diffraction loss negligible for a confocal Fabry-Perot resonator, the mirror radius should be

greater than $0.9(b\lambda)^{-1/2}$. Semi-confocal resonators with Fresnel numbers larger than ~0.8 incur approximately two orders of magnitude greater diffraction losses than the confocal geometry using the same size mirrors [53]. This is not as severe a performance issue as it may initially appear. The rapid fall-off in diffraction loss with increasing mirror size causes a semi-confocal resonator with $N = 1.2$ to achieve roughly the same diffraction performance as the confocal resonator with $N = 0.8$. Therefore an increase in mirror radius of 20% to 30% will give a semi-confocal resonator the same diffraction performance, and hence the same Q as a confocal resonator with smaller ($r = 0.9(b\lambda)^{-1/2}$) mirrors.

Investigating the sensitivity of resonator Q to small changes in the intermirror distance requires substituting the explicit expressions for α_D, α_i, and α_r into the previous equation for Q and using implicit differentiation with respect to b. The resulting equation gives change in Q due to a small change in b, for a resonance with mode order $[n,m,p]$

$$\frac{dQ}{db} = \frac{Q^2}{b}\left\{\left[2\left(1-\pi m_o\frac{a^2}{b^2}\right)\right]\frac{1}{Q_D}+\frac{1}{2Q_i}+\left[\left(\frac{f_{n,m,p}}{\alpha_r}\right)\frac{d\alpha_r}{df_{n,m,p}}\right]\frac{1}{Q_r}\right\}, \qquad \textbf{(58)}$$

where $m_o = (1 + 2p + m + n)$ is the mode order factor and $d\alpha_r/df_{n,m,p}$ is the frequency dependence of coupling losses. This equation shows that the change in Q depends on several specific details of resonator design and operation. Later in the design process sensitivities of Q to dimensions of the candidate resonator designs and operating modes can be analyzed with this expression. This completes the general development for Fabry-Perot resonators.

F. Measurement Electronics

Accurately determining the Q of a resonator filled with moist air requires measurements of resonator frequency, amplitude, and bandwidth. Figure 4 depicts a possible measurement system with those capabilities. A frequency synthesizer locked to a precision frequency standard provides the signal source. Source stability must exceed the intrinsic cavity stability and its linewidth must be smaller than the resonator bandwidth times the accuracy requirements. Stability requirements will be discussed later because they depend on parameters such as measurement accuracy, sampling duration, and gas absorptivity. The synthesizer frequency is controlled by a computer which monitors the spectrum analyzer output. It is programmed to sweep over a given frequency range until it detects a peak in resonator power. The spectrum analyzer then directs the synthesizer to sweep spectral regions spanning the resonance peak and -3 dB points, recording both frequency and

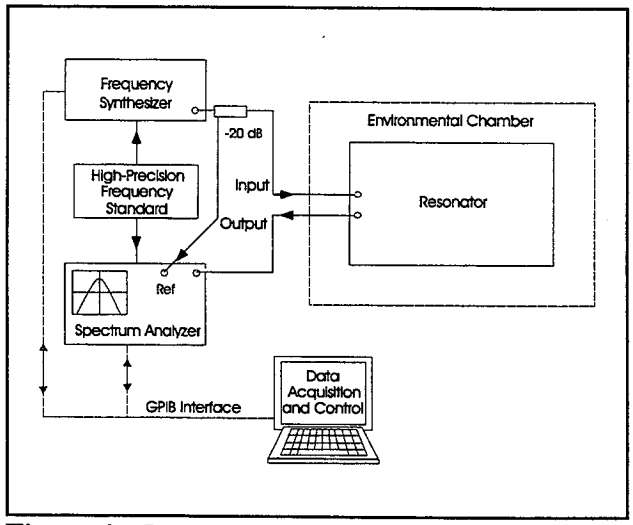

Figure 4. *Resonator Measurement System Block Diagram*

amplitude. The measurement cycle duration is the time required to sweep all three regions. All information transmitted by the spectrum analyzer and synthesizer is recorded by the data acquisition system and stored on disk. Another possible implementation would use a phase-locked detection scheme in place of the spectrum analyzer.

There are several techniques for coupling electromagnetic signals into and out of a resonator. For this application weak coupling is required to prevent significant reduction in Q. Traditional high-bandwidth methods include tapered horn feeds, small apertures, and multiple slots. A relatively new coupling technique uses a coaxial feed with a small movable loop antenna inside an aperture port [3] as shown in figure 5. This technique provides larger bandwidth than waveguide feed systems, as well as adjustable coupling via adjustment of the loop's position in the port. The port consists of a cylindrical hole in the resonator wall material, with a constricted iris at the end adjacent to the resonator interior. Its diameter should be small compared to the signal wavelength so the port acts as a circular waveguide below the cutoff frequency. The loop antenna is smaller in diameter than the port, and is fashioned from the center conductor of the coaxial cable feeding the resonator. A sliding metal bulkhead inside the port is soldered to the coaxial cable outer conductor immediately behind the loop. This bulkhead serves to center the loop within the port and prevents propagation behind the loop, away from the resonator cavity. The adjustable distance between the iris and antenna loop controls the resonator coupling, so the resulting degradation in Q can be reduced to acceptable levels. The iris aperture size determines maximum coupling. A simple mechanism such as illustrated in figure 5 can advance, retract, or secure the coax-bulkhead-loop assembly.

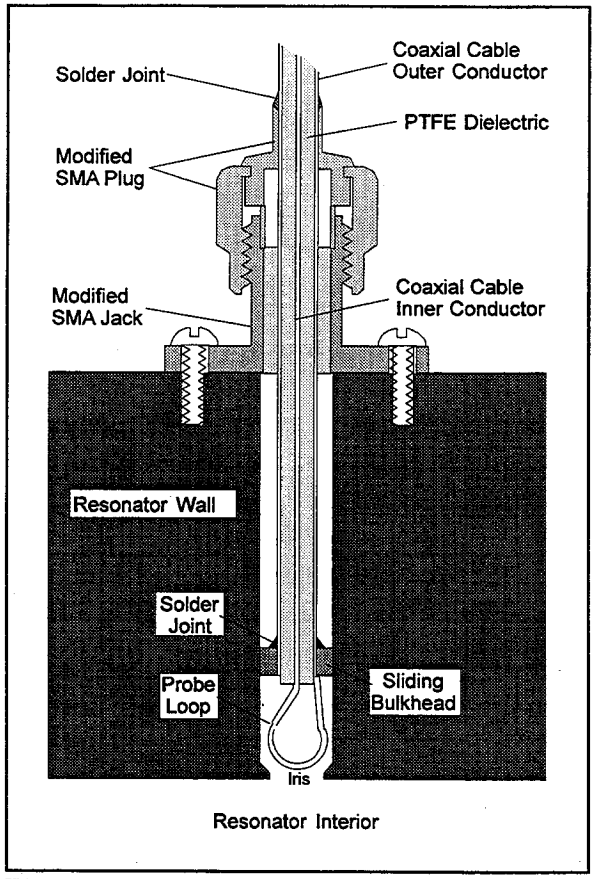

Figure 5. *Coax-fed Adjustable Loop Antenna for Coupling Signals In and Out of the Resonator (After Spilker [3])*

It has been suggested that greater mode isolation could be achieved by injecting only the eigenmode of interest (H. Pickett, pers. comm). Consideration was given to arranging phased array antenna elements on a wall of a rectangular cavity resonator to preselect coupling to specific modes. Preliminary analysis indicates this approach has merit. But since resonance mode spacing as well as the efficiency, impedance, and bandwidth of a given coupling method depend on cavity design details, this issue is best decided later in the design process, after a cavity design has been finalized. At that time, the performance of various candidate feeds can be predicted using electromagnetic analysis code.

G. Frequency Measurement Accuracy for Single-Mode Resonators

The accuracy of refraction and absorption determinations using a single-mode resonator depends on the accuracies of full-width, half-maximum (FWHM) bandwidth, Δf, and center frequency, f_c, measurements. These quantities can be derived from the "-3 dB points," f^+ and f^-, which are the frequencies above and below the center frequency, respectively, at which the resonator power drops 3 dB below peak power. Assuming a symmetric resonance shape,

$$f_c = \frac{f^+ + f^-}{2} \quad , \tag{59}$$

$$\Delta f = f^+ - f^- \quad . \tag{60}$$

Uncertainties in measurement of f^+ and f^- directly translate into uncertainties in refractivity and absorptivity.

A source of measurement uncertainty is the random error introduced by a finite frequency measurement period. When a frequency is measured by a frequency counter, the measured frequency is uncertain by the truncated parts of the waveform at the beginning and end of the counting period. The uncertainty in f is

$$\delta f_i = \frac{1}{\tau_{int}} \quad , \tag{61}$$

where τ_{int} is the "integration period" or counting period. For a τ_{int} of 0.1 seconds, the frequency measurement error is 10 Hz. Reference oscillators that are stable to slightly better than one part in 10^{10} over periods of seconds are readily available. Therefore, for the range of microwave frequencies of interest and periods on the order of several tenths of a second, these errors will usually exceed errors introduced by drifts in a quartz reference oscillator. For example, at 25 GHz, one part in 10^{10} corresponds to 2.5 Hz which corresponds to an 0.4 second counting period. When a quartz oscillator is slaved to an atomic standard, the long term accuracy (> 10 seconds) can be improved by more than an order of magnitude.

Uncertainties in measuring power also pose a significant source of error. An error in the -3 dB power measurement translates into a frequency error in both f^+ and f^-. The size of the frequency error depends on the slope of the resonance frequency response at the point where the frequency measurement is attempted. Assuming a standard Lorentzian shape, the resonator response curve is

$$P(f) = \frac{P_o}{1 + \frac{(f - f_c)^2}{(\Delta f/2)^2}} = \frac{P_o(\Delta f)^2}{\Delta f^2 + 4(f - f_c)^2} \tag{62}$$

where f is frequency and P_o is the peak power measured at the center frequency f_c. An expression of this in decibels is

$$P^*(f) = P_o^* + 20 \log_{10}\Delta f - 10 \log_{10}\left(\Delta f^2 + 4(f - f_c)^2\right) \quad , \tag{63}$$

using

$$P_o^* = 10 \log_{10} P_o \quad . \tag{64}$$

The derivative with respect to f yields the sensitivity of frequency measurements to power measurements

$$\frac{dP^*(f)}{df} = \frac{-80}{\ln 10}\left(\frac{f - f_c}{\Delta f^2 + 4(f - f_c)^2}\right) \quad . \tag{65}$$

A power measurement error δP^* will induce a frequency measurement error δf_p:

$$\delta f_p = \frac{\delta P^*}{dP^*/df} \quad , \tag{66}$$

with the derivative in the denominator evaluated at f^+ or f^-, as appropriate.

The total measurement error is the sum of counting period error δf_c plus the power measurement error, δf_p. The measured frequencies f_m^- and f_m^+ are written as actual -3 dB frequencies plus the measurement errors

$$f_m^- = f^- + \delta f_p^- + \delta f_i^- \quad , \tag{67}$$

$$f_m^+ = f^+ + \delta f_p^+ + \delta f_i^+ \quad . \tag{68}$$

Using these values to calculate the measured center frequency $f_{c,m}$ yields

$$f_{c,m} = \frac{f_m^- + f_m^+}{2} = f_c + \frac{\delta P^{*-} - \delta P^{*+}}{2[dP/df]_{f=f^-}} + \frac{\delta f_i^- + \delta f_i^+}{2} \quad . \tag{69}$$

(Note that $[dP/df]_{f=f^-} = -[dP/df]_{f=f^+}$.) If the counting error and the power error are random they can be reduced by averaging. However, a worst case analysis can be calculated for a single measurement or repeated measurements where both the power and counting errors are assumed to be correlated and systematic. The counting error term δf_i is maximized when δf_i^- and δf_i^+ are of magnitude $1/\tau_{int}$ and have the same signs. The maximum instrumental power error, ε_p, is

determined by the signal analyzer used to make the power measurements. When δP^{*+} and δP^{*-} have opposite signs and a magnitude of ε_p then the total power error is maximized. The maximum error in the center frequency occurs when the total power error and counting error have the same sign. Therefore, at the low frequency -3 dB point, $f = f^-$, $(f - f_c) = -\Delta f/2$ and $[dP/df]_{f=f^-} = 20/(\Delta f \ln 10) \approx 1/0.115\Delta f$, and

$$\delta f_c = f_{c,m} - f_c = 0.115\Delta f \varepsilon_p + \frac{1}{\tau_{int}} \quad . \tag{70}$$

The counting term can be reduced by increasing the integration time. Reducing the magnitude of the power error term requires reducing Δf since there is a hardware limit on ε_p. The bandwidth Δf is determined by the resonance center frequency and Q, $\Delta f = f_c/Q$, so maximizing Q will minimize the power error. This makes physical sense, since the higher the Q, the narrower the bandwidth and the steeper the power versus frequency curve in the region of the -3 dB power points. A large Q causes a large error in power to translate into a small frequency error.

The absolute accuracy that can be achieved by spectrum or network analyzers is slightly better than 0.02 dB [42]. The precision of a power measurement that is made in the range of 10 dB to 20 dB below the reference signal level (resonator input) is approximately 0.003 dB [42]. Assuming a resonator with a Q of 10^6 at f_c = 25 GHz, the resonance bandwidth will be 25 kHz. Combining these assumptions with τ_{int} = 0.1 seconds and ε_p = 0.005 dB, the maximum single center frequency measurement error would be 24 Hz.

The impact of power and counting errors on refractivity determinations can now be assessed. As shown in section IV.C, the index of refraction n is the ratio of the center frequency of an evacuated resonator, f_{cv}, to its center frequency when loaded, f_{cl}. For gases under atmospheric conditions $n = f_{cv}/f_{cl} \approx 1$, so $f_{cl}/f_{cv} \approx 1$. Therefore the effect of errors in frequency measurements can be calculated by taking the total derivative of Equation 17 with respect to the two frequency measurements

$$\left|\frac{\delta n}{n}\right|_{\max} \approx \left|\frac{\delta f_{cv}}{f_{cv}}\right|_{\max} + \left|\frac{\delta f_{cl}}{f_{cl}}\right|_{\max} \approx \frac{|\delta f_{cv}|_{\max} + |\delta f_{cl}|_{\max}}{f_{cl}} \quad . \tag{71}$$

The refractivity error, δN, can then be written

$$\left|\frac{\delta N}{N}\right|_{\max} \approx \frac{|\delta f_{cl}|_{\max} + |\delta f_{cv}|_{\max}}{f_{cv} - f_{cl}} \quad . \tag{72}$$

A 24 Hz frequency error at 25 GHz corresponds to approximately 10^{-9} error in the index of refraction. At a wide range of lower atmospheric pressures and humidities, the uncertainty in refractivity between 18 and 35 GHz will range between 10^{-4} and 10^{-6}, with higher accuracy estimates corresponding to gas samples at higher pressures and humidities. It can be concluded that uncertainties in measuring the frequency shift do not limit the accuracy of refractivity determinations.

As discussed earlier, absorptivity measurements rely on measuring the increase in resonator bandwidth induced by introducing gas into an evacuated resonator. The measured bandwidth Δf_m is the sum of the actual bandwidth Δf plus the measurement error $\delta(\Delta f)$ and can be calculated from the measured frequencies of the -3 dB points:

$$\Delta f_m = \Delta f + \delta(\Delta f) = f_m^+ - f_m^- \tag{73}$$

$$\Delta f_m = \Delta f + \frac{\delta P^{*+} + \delta P^{*-}}{[dP/df]_{f=f^-}} + \delta f_i^+ - \delta f_i^- \quad . \tag{74}$$

The worst-case error occurs when these errors have the same magnitudes as in the refractivity case but opposite signs, yielding

$$\delta(\Delta f) = 2\left(0.115\Delta f\varepsilon_p + \frac{1}{\tau_{int}}\right) \quad . \tag{75}$$

Since the bandwidth error scales with the bandwidth, measurement errors are decreased by increasing resonator Q.

Absorptivities can be calculated from measured bandwidths using Equation 34

$$\alpha = \pi\frac{n}{c}(\Delta f_{m,l} - \Delta f_{m,u}) \quad . \tag{76}$$

where $\Delta f_{m,l}$ is the loaded resonator bandwidth and $\Delta f_{m,u}$ is the bandwidth of a resonator with a nonabsorptive load. Remember the nonabsorptive load is picked so that its refractivity is matched to that of the atmospheric gas sample. Also this expression needs to be multiplied by 20 $\log_{10}e$ to convert α to units of dB per unit length. The quantity in parentheses is the bandwidth difference, Δf_d. Each bandwidth measurement used to determine Δf has an uncertainty of $\delta(\Delta f)$, so the absorptivity measurement has uncertainty

$$\delta\alpha = \frac{2\pi n}{c}\delta(\Delta f) = \frac{4\pi n}{c}\left[0.115\Delta f\varepsilon_p + \frac{1}{\tau_{int}}\right] \tag{77}$$

Measuring the expected absorptivities to 1% accuracy will be more challenging than refractivity measurements. Moist air measurements with absorptivity α of 0.5 dB/km require an absorptivity error $\delta\alpha$ of 0.005 dB/km, so $\delta(\Delta f)$ must be held to 28 Hz or less for 1.0% accuracy. For absorptivity measurements, only the relative power difference between the peak power and the -3 dB point is necessary, so the instrumental precision (and not accuracy) is relevant for this measurement. Using Δf = 25 kHz and ε_p = 0.005 dB, the power term alone equals the error budget with a contribution to $\delta(\Delta f)$ of 29 Hz. With τ_{int} of 0.1 sec the counting error term contributes another 20 Hz which, together with the power term exceeds the error budget. Increasing τ_{int} to 0.25 seconds decreases its contribution from 20 Hz to 8 Hz which corresponds to a $\delta\alpha$ of 0.0015 dB/km. To bring the sum of the errors to within the error budget allocation requires increasing the cavity Q to 1.5×10^6.

These analyses demonstrate that the measurement error corresponding to reasonable values of resonator Q, measurement frequencies, and a range of interesting absorptivities will have single-measurement accuracies ranging from 0.5% to 10% assuming that power measurement errors and counting errors are correlated and systematic. In contrast, refractivities can be determined much more accurately, better than a part in 10^4 (usually much better) for all cases. Improvements that can be obtained from multiple measurements have not been considered because of the need for assumptions about error source randomness and correlation. It would help to make a careful analysis of a specific instrumental setup to allow constraints to be placed on the randomness of the counting and frequency error. To solidify an estimate of accuracy improvements that can be obtained from multiple measurements requires that assumptions regarding randomness of the resonator measurement error be tested. This turns out to be straightforward. The refractivity of nitrogen, argon, and oxygen are independently known to 0.1% or better. Therefore repeated refractivity measurements made on these gases will allow compilation of statistics on the accuracy to which the -3 dB power points can be measured. Also since argon and nitrogen are listless gases, bandwidth measurements can be collected on argon, nitrogen, and the evacuated resonator looking for anticorrelations during measurement of the -3 dB power points. These two types of measurements will allow the randomness of the errors to be tested to 0.1% or better. They will also allow investigation of systematic changes in cavity bandwidth and center frequency as a function of pressure, internal medium, and frequency to the 0.1% level or better. These tests will allow the total multiple-measurement error to be driven down to the 0.1% level.

H. Multimode Cavity Resonators

Water vapor absorptivity can be measured with a multimode resonator [4]. But unlike single mode techniques, multimode methods aren't capable of refractivity measurements. Also, they provide less of the diagnostic information that is essential in tracking systematic error sources. Because multimode techniques have been used in the past and proposed for the future, it is important to understand inherent limitations to their accuracy.

Since Becker and Autler [4] made their water vapor measurements using a multimode cavity resonator, it is worth analyzing their apparatus. They constructed an approximately cubic, 15.8 m^3 multimode cavity. It was energized at 11 frequencies, from 17.8 to 40 GHz with 0.25 to 0.5 μs pulses with peak powers ranging from 10 to 40 kW. A 2/3 meter diameter fan in front of the input signal aperture "mixed" the microwave modes to promote a uniform average field distribution. They inferred changes in the average field strength inside the cavity (and thus changes in the stored energy and Q) from temperature changes in thermocouples inside the cavity. The thermocouples had been coated with a microwave absorbing mixture, so their temperature deviations from cavity ambient were directly related to the microwave field strength. Their array of 360 thermocouples located throughout the cavity helped ensure that the average field strength sampled by the array was not significantly different from the true average field strength inside the cavity. Absorptivity of the cavity's internal medium was calculated once a relation between radiation-induced temperature changes and resonator Q was established.

The change in Q due to a gas load can be determined by comparison to the change in Q due to opening a calibrated aperture in the cavity wall [4]. Like the single mode case, the observed Q of a multimode resonator can be related to a sum of contributions from various loss sources: Q_i, the intrinsic Q, includes losses from walls, thermocouples, fan, etc.; Q_g is associated with the load; and Q_r includes radiative losses from cavity apertures, notably from the calibrated aperture. It is useful to separate Q_r into two terms, a calibrated aperture term, Q_a, and a term, $Q_{r'}$ that represents all other sources of radiative losses, then

$$\frac{1}{Q} = \frac{1}{Q_i} + \frac{1}{Q_{r'}} + \frac{1}{Q_a} + \frac{1}{Q_g} \quad . \tag{78}$$

The calibrated aperture must be small compared to the cavity wall area but large enough that diffraction effects are insignificant [4]. The Q of this aperture is simply

$$Q_a = \frac{8\pi V}{\lambda A} \quad , \tag{79}$$

where V is the cavity volume, A is the aperture area, and λ is the radiation wavelength [54]. The Q of the load is given by

$$\frac{1}{Q_g} = K\gamma\lambda \tag{80}$$

where γ is the absorption coefficient in logarithmic units and K is a constant of proportionality that depends on the units. To determine Q_g, the thermocouple output was measured with the aperture closed and then with it open [4]. For an initial load of dry air, the change in heating for the open and closed aperture calibrated the relationship between thermocouple output and Q. This calibration was then applied to the change in thermocouple output when the dry air in the cavity was replaced by wet air. The indicated change in the observed Q was then used to calculate Q_g, which yielded the wet air absorptivity. In practice there are many ways to provide a calibrated change in Q, such as introducing a calibrated dielectric load into the cavity or making a precise dimensional change, but the relationships between Q and these other parameters are valid only when the fields in the cavity are uniform due to simultaneous excitation of a large number of modes [5].

Becker and Autler tried another method for determining Q [54]. They energized the cavity with microwave pulses and attempted to determine the rate of energy loss. As discussed earlier, Q is the constant of proportionality for the rate of field damping. But Becker and Autler were unsuccessful because of enormous unexplained power fluctuations while the fields decayed. Although they weren't able to definitively ascertain the cause, it was probably caused by mode "hopping" (coupling of energy back and forth between modes) or spatial interference between the modes resulting from thermal and vibration-induced cavity deformations.

As stated earlier, there are more sources of systematic errors inherent in multimode resonators than in single mode resonators, with fewer diagnostics to investigate them. For example, with single mode resonators, absorption can be independently calculated from power and frequency measurements, providing a cross-checking capability that is not available from multimode systems. Additionally, single mode resonance shapes, unavailable from multimode systems, carry useful diagnostic information. Multimode measurements rely on comparisons with a calibrated change in Q as discussed above. This makes accuracies of Q determinations, and thus absorption measurements, highly dependent on calibration accuracy, linearity of Q with load, and electromagnetic field uniformity within the cavity. Field uniformity is exceedingly difficult to measure in a multimode resonator. But without empirical measurements on the actual cavity used for the absorption measurements, its effect on measurement accuracy is difficult to predict.

Single mode resonators have several other important advantages over multimode resonators. Their refractive measurement capability provides a check on environmental sensors. Single mode frequency measurements are useful for characterizing thermal induced cavity deformations. Use of a single mode ensures that Q is not affected by mode hopping. Finally, single mode systems do not require mechanical mode-mixing devices which create pressure differentials and other side effects that hamper environmental control and cavity stability. The conclusion is that the high level of accuracy desired, and the significant advantages of single mode spectrometers over multimode systems, make multimode measurements inappropriate.

I. Preliminary Recommendations

These discussions of spectroscopic techniques are useful in choosing the one that is best suited to determine atmospheric gas absorptivities. At the outset, absorption cell techniques can be rejected because they are not capable of the requisite accuracy. Multimode resonators can be dismissed because their measurement accuracy is restricted by the limited amount of diagnostics they provide. This reduces the possible candidates to the single-mode rectangular cavity resonator and the Fabry-Perot resonator. The best choice hinges on a comparison of their potential accuracies, ease of fabrication, difficulty in controlling their internal environments, and estimated costs.

The relative change in resonator bandwidth and power ratio induced by a gas sample increases with Q. For a given resonator geometry and choice of construction material (which determines wall resistivity or mirror reflectivity), Q can only be increased by making the resonator larger. However, increasing the resonator's volume will make it more difficult to fabricate, harder to control the internal environment, and more sensitive to temperature-induced changes in the cavity dimensions. Hence, increasing resonator volume will increase costs.

Q is proportional to the ratio of the resonator's volume to its surface area. Therefore, a rectangular cavity has a maximum Q when all sides are equal length; in other words, when it is a cube. For this case, both the TE and TM modes reduce to the same expression for Q

$$\frac{1}{Q} = \frac{4\delta}{a} + \frac{1}{Q_r} \quad . \tag{81}$$

Using $\delta = (\pi f \mu \sigma)^{-1/2}$ [44] and $c\mu = \eta$, the Q for the Fabry-Perot resonator can be rewritten

$$\frac{1}{Q} = \frac{\lambda}{2\pi b}\sqrt{\frac{\pi}{\eta\sigma\lambda}} + \frac{1}{Q_r} + \frac{1}{Q_D} = \frac{\delta}{2b} + \frac{1}{Q_r} + \frac{1}{Q_D} \quad . \tag{82}$$

The volume of the cubic cavity is a^3. This can be equated with the volume of the cylindrical, confocal Fabry-Perot cavity which is approximately $\pi b^3/4$. Assuming the diffraction losses and radiative losses are negligible, the ratio of the Q's of the two different geometries are

$$\frac{Q_{cube}}{Q_{Fabry-Perot}} \approx \frac{a}{8b} \approx \frac{1}{8.7} \quad . \tag{83}$$

Therefore for a given volume, use of the Fabry-Perot geometry gains nearly a factor of 9 in Q. This supports the use of the Fabry-Perot geometry.

As was just mentioned, for a given Q, a smaller resonator will experience a smaller change in size due to a temperature change. The Fabry Perot resonator scores another advantage in its thermal stabilization requirements. It only requires stabilization of the intermirror distance, whereas a rectangular cavity is sensitive to all three sets of interwall spacings. Thus, a rectangular cavity will require that its structure have thermal compensation along three axes instead of one.

Environmental control, which will be discussed in the next section, is simplified with the Fabry-Perot resonator. The open structure makes it simpler to mix and change gas samples in the measurement area. In contrast, the rectangular cavity needs a series of ports and outlets to keep the gas well mixed. Also, the presence of monitoring probes inside the rectangular cavity will reduce the cavity's Q.

Finally, the cost of a rectangular cavity is not much less than that of the Fabry-Perot resonator. In fact, the expense of fabricating one or two spherical mirrors for a Fabry-Perot geometry will be more than offset by the combination of the rectangular cavity's increased size, extra environmental control system capacity, and the need for three axes of thermal compensation.

In conclusion, this comparison supports a recommendation that a single-mode, confocal or semi-confocal Fabry-Perot resonator be used to measure the absorptivity of atmospheric gases.

V. Environmental Monitoring and Control

A. Overview

The microwave spectrometer will need to operate within an environmental chamber. This chamber should be able to provide a pressure range of 0.1 to 120 kPa, a temperature range of -5 to 30 °C, and a humidity range of 0 to 80%. Its dimensions will be governed by the size and radio properties of the spectrometer. In general, the spectrometer can be isolated from the environmental chamber by designing a chamber large enough to ensure that its walls are many wavelengths from the spectrometer's active area. Coupling between the environmental chamber and spectrometer can be modeled using commercial CAE electromagnetic field simulation code. Finally, the spectrometer requires a moderate level of isolation from seismic noise to prevent microphonics from generating spurious signals. This can be achieved with a combination of rubber floor pads, paying careful attention to how the spectrometer is mounted within the chamber, and an appropriate choice of location. In fact, it would be desirable to house this experiment in a lab that already has been isolated from building vibration.

B. Measurement Accuracy

Measurement accuracy for environmental parameters inside the microwave spectrometer sets a limit on the accuracy of absorption coefficient determinations. Pressure, temperature, and humidity measurements provide data required to correlate the gas sample's thermodynamic state with its absorptivity. Accurate environmental sensing furnishes a critical diagnostic for verifying and monitoring the chamber's regulation and spectrometer performance. A resource for ensuring sensor accuracy is the JPL instrument calibration and standards laboratory (JPL section 375). Their calibration techniques and standards are directly traceable to National Institute of Standards and Technology (NIST).

A standard for temperature measurements in the United States is the standard platinum resistance thermometer (SPRT) which is maintained by NIST [55]. SPRTs are capable of ±0.3 mK repeatability with a total uncertainty of ±1 mK. An SPRT traceable to NIST costs several thousands of dollars. Platinum resistance thermometer sensors with absolute accuracies of ±10 mK can be purchased for $500 to $800 and only require a digital multimeter to operate. These thermometers could then be recalibrated at JPL improving their absolute accuracy at least four-fold. At room temperature, a 10 mK temperature error represents less than 0.004% total error.

The NIST standard for pressure is accurate to 0.0022% between 21 kPa and 103 kPa [55]. The standard gauges have stated accuracies of 0.005 to 0.01 kPa. However, pressure gauges with absolute accuracies of 0.05 kPa can be purchased for two to four thousand dollars. As in the case of thermometers, a NIST traceable calibration of pressure gauges can be made at JPL. At 20 kPa, the lowest pressure in the specified measurement range, an error of 0.05 kPa represents 0.25% error. Lower pressures (~0.1 kPa) will needed to evacuate the chamber between data runs; however, these pressures will not require accurate measurement.

Humidity will be the most challenging parameter to measure accurately. The NIST standard for relative humidity is 0.4% with ambient temperatures ranging from -20 °C to 0 °C and 0.2% with ambient temperatures between 0 °C and 60 °C [55]. NIST also provides a standard for dewpoint which is accurate to ±0.04 °C between -35 °C to 60 °C. In order to ensure humidity accuracy several technologies should be employed.

Chilled mirror hygrometers have high accuracies at low to moderate relative humidities with costs between two and eight thousand dollars. They make measurements by cooling a tiny mirror until a layer of frost or dew forms. This temperature is the frost or dew point and can be directly measured with an accuracy of up to ±0.1 °C.

The calibration facility at JPL can provide NIST traceable calibrations of humidity at ambient pressure with accuracies of ±0.5%. There is a facility in New Mexico that has a copy of the NIST humidity standards chamber which provides higher calibration accuracy and operates over a wide range of pressures. In the final analysis, it is believed that water vapor can be measured to an accuracy of better than ±1.5% over the range of humidities, pressures, and temperatures specified in this experiment. However, the accuracy of water vapor measurements will range from 0.5% to 1.0% in the thermodynamic range where the majority of the delay occurs (i.e., conditions in the bottom two kilometers of the atmosphere).

C. Environmental Control

Environmental control can be achieved using either a flowing gas or stagnant air system. A flowing gas system would maintain a constant flow of humid air through the resonator. This would allow rapid changes in the gas sample's thermodynamic state, but requires precise regulation of gas pressure, temperature, humidity, and flow rate. In contrast, a stagnant air system requires a sequence of steps to generate the gas sample. The measurement cycle starts with evacuating the vacuum chamber. After vacuum is achieved ($\leq$ 0.1 kPa), the vacuum system is sealed and the sample gas can be introduced. When the sample has equilibrated, its thermodynamic state is measured while the microwave absorption measurements are made. Before reevacuating the chamber and initiating a new measurement cycle, the gas inside the chamber can be altered by adding more gas. This will reduce the amount of time it takes to span a wide range of thermodynamic states. Stagnant air systems decrease sample variability and reduce thermodynamic gradients allowing greater measurement accuracy (Bob Hardy, pers. comm.). They also eliminate the vibrations and microphonics caused by a gas flow. Hence, a stagnant air environmental control system is preferred for these measurements. A stagnant air environmental controller will require a vacuum chamber, a vacuum system, and a gas delivery system.

The vacuum chamber houses the resonator and environmental sensors. The range of pressure for absorptivity measurements spans from 20 to 120 kPa. However, the ability to evacuate the chamber to 0.1 kPa between data runs is required to ensure the integrity of the gas sample. As mentioned earlier, the chamber's dimensions are determined by the resonator. The chamber will need to be fitted with a series of vacuum quality electrical and radio frequency (RF) feed-thru's,

mechanical actuators, windows, and valves. Fans should be installed inside the chamber to keep the air mixed and ensure that the gas temperature is uniform. To minimize pressure gradients and vibrations, fans must be turned off during the actual microwave measurements.

Condensation of water on the walls of a resonator can cause systematic errors. Deposition of a thin layer of liquid water on a cavity wall changes its surface impedance, which in turn changes resonator Q. Various wall coatings to minimize adsorption have been investigated [56]; however, none yielded significant reductions in condensation. Two other approaches have provided some success at minimizing condensation: heating the mirrors 1 K above the ambient temperature and restricting measurements to relative humidities below ~75% [56]. Since heating the mirrors could introduce systematic errors and hence needs more investigation, reducing the range of maximum humidities could provide an acceptable solution. Boudouris [37] showed that the refractivity data could be used as a diagnostic to determine the condensation point. At high humidities, deviations of measured refractivities from theoretical predictions can be used to verify that vapor condensation is corrupting the absorptivity data.

Precise temperature control of the environmental chamber can be attained by circulating a high heat capacity fluid through an insulated jacket surrounding the vacuum chamber [57]. Also, the fluid should also be circulated through heat exchangers in the gas delivery system to equilibrate the gas temperature to the chamber temperature. The difference in temperature between the fluid entering the chamber jacket and returning to the fluid reservoir can be used to servo the heater/cooler that services the temperature-control fluid reservoir. The time required for thermal equilibrium depends on the insulation, size of the chamber, fluid flow rate, and servo gain. Using a water-glycol mix, this method has demonstrated 20 mK temperature stability [57].

The range of vacuum pressures required for this application can be handled by a mechanical pump [58]. Pumping humid air can rapidly contaminate vacuum pump oil [58], so a gas ballast rotary pump is needed to prevent water condensation within the pump. Such a pump can achieve pressures of 10^{-3} kPa, which exceeds the needs of this application [59]. Pumping speeds can be calculated by

$$t = \frac{V}{S} \ln\left(\frac{P_1}{P_2}\right) \quad , \tag{84}$$

where t is time in seconds, V is the volume of the vacuum system in liters, S is the pumping speed in liters per second, P_1 is the initial pressure, and P_2 is the final pressure [58].

Supplying a well-characterized gas sample to the resonator requires a precision gas source. Although initial measurements can be made with filtered room air, precision gas samples are commercially available which are NIST-traceable [60]. Atmospheric gas mixtures meeting primary standards carry certifications which specify the O_2 and N_2 content with ± 0.02% accuracy and specify carbon dioxide, argon, and other trace gases concentrations to 1% accuracy [60]. Since the partial pressure of oxygen is only needed to slightly better than 1%, this gas standard is more than adequate. In fact, it may be possible to substitute a less expensive grade of gases

for these measurements. Finally it may be desirable to use CO_2-free gas. During humidification, CO_2 can be dissolved in the water baths forming carbonic acid, (H_2CO_3), depleting the CO_2 content [61]. Any discrepancies between gas concentrations used for measurements and natural abundances need to be corrected during analysis [62, 63].

The gas sample can be humidified with a series of water baths and heat exchangers as depicted in Figure 6. This is a simplified version of the humidity system used as a NIST standard [62], [63, 64]. Initially the air sample is passed through a flow meter and regulator to a heated presaturator water bath. The temperature of the water is 10 to 15 K warmer than the desired saturation temperature (dew point temperature). The air enters the bath slightly above the water level and its flow is directed at the water surface. It then passes through a series of heat exchangers set at the environmental chamber temperature and enters a final water bath humidifier which is set at the saturation temperature. Again the air is deflected into the water surface. The humid air now passes through an expansion valve which can be used to set the relative humidity. Changing the temperature of the various baths and altering the expansion valve flow rate allows a wide range of humidities to be generated. It is possible that the dual humidifiers are unnecessary, and that a single humidifier is adequate. Remember, this experiment only requires that measurements be made on a wide range of well-known humidities, it does not require generation of predetermined humidities that have been specified with high accuracy.

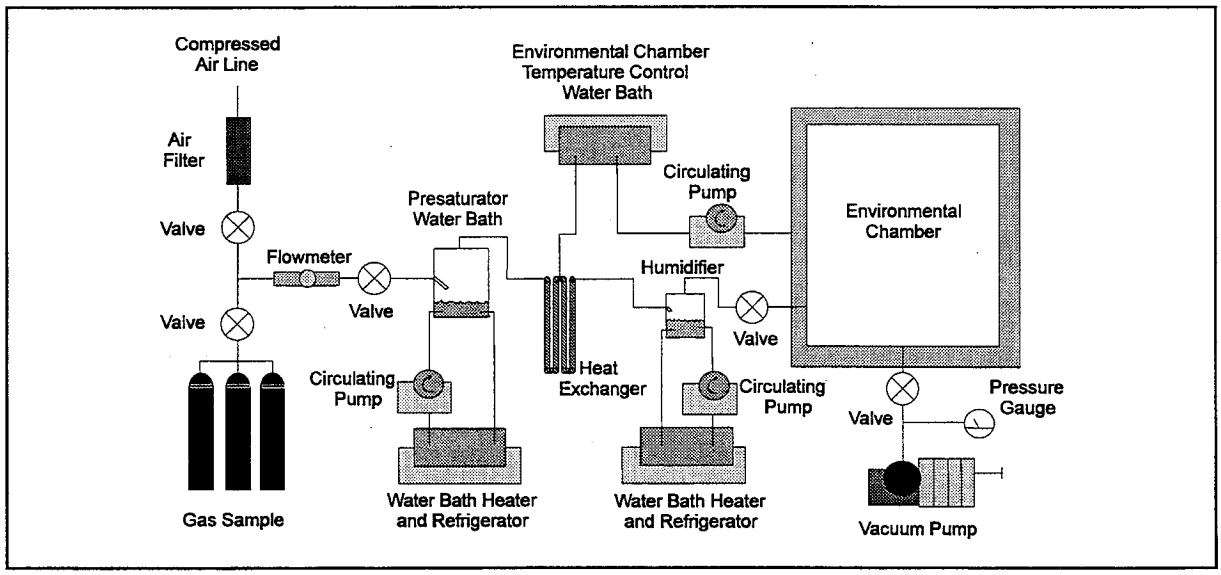

Figure 6. *Environmental Control System*

D. Thermally Compensating the Resonator Structure

Deformations in resonator shape can produce systematic errors in absorptivity determinations. Such deformations are primarily driven by thermal fluctuations. These changes can be controlled by both tightly controlling the environmental chamber's temperature and thermally compensating

the resonator structure. Both active and passive techniques exist to minimize the impact of thermal perturbations on resonator frequency and Q. Active systems tend to be expensive because they require additional measurement apparatus as well as active positioners. Passive compensation can often be implemented at much lower cost.

Modeling passive techniques for minimizing temperature-induced deformations requires the linear approximation of the relationship between dimensional and temperature changes

$$\Delta L = \alpha L_o \Delta T \ , \quad for \ \Delta T \ll T_{ambient} \quad , \tag{85}$$

using ΔL to represent change in length, L_o as the unperturbed length, ΔT as change in temperature, and α as the thermal expansion coefficient [65]. For larger temperature changes a second term of the form $\beta L_o(\Delta T)^2$ could be added to improve accuracy. Table 3 lists the expansion coefficients for various materials. The primary strategy for minimizing thermal perturbations is to construct the resonator out of a material with a low coefficient of thermal expansion such as invar or fused quartz. Designing thermal compensation into the structure can achieve additional improvement.

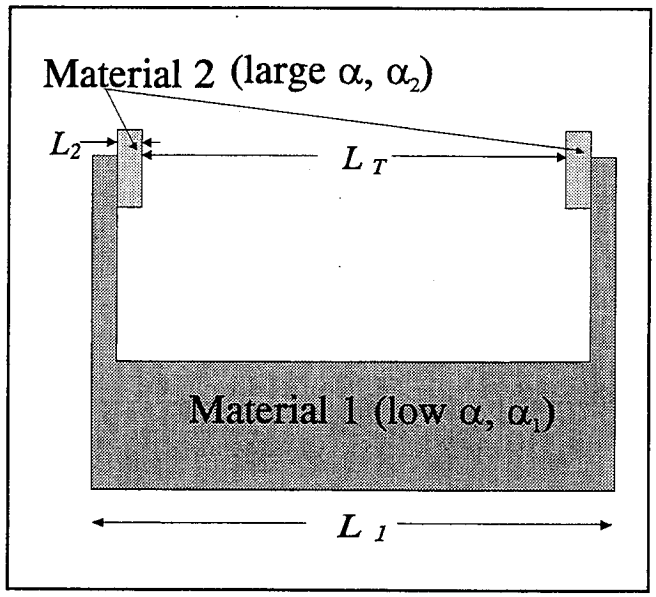

Figure 7. *Example of an Athermalized Structure.*

Thermal compensation of a structure is best illustrated with an example, such as depicted in Figure 7. In this example, compensation will minimize changes in the dimension designated L_T. As shown, thin pieces of material with a large expansion coefficient have been placed on each end of a larger U-shaped frame constructed of a low expansion material. When the outer frame expands with increasing temperature, the thin blocks expand inward counteracting the change in L_T. Deriving the relationship for perfect compensation requires setting the ΔL_i values equal to each other, yielding the relationship

$$\alpha_1 L_1 = 2\alpha_2 L_2 \quad . \tag{86}$$

This can be implemented in a rectangular cavity by inserting aluminum blocks between the cavity walls and its outer invar support structure. Similarly, mirrors for a Fabry-Perot resonator can be fixed to aluminum blocks which are fastened to an invar frame.

Measurements of resonator frequency shifts can be used to tune a compensated structure. With a non-absorptive load, the temperature can be cycled over tens of degrees. Measured changes in cavity eigenfrequency can then be used to determine the net resonator expansion coefficient. Thicknesses of the compensating shims can be modified accordingly.

Finally, it has been suggested that the resonator support frame be constructed using layered composite materials (R. Linfield, pers. comm.). Although composite structures have been developed with very small thermal coefficients they would be inappropriate for this application. Successful realization of an athermalized composite structure is difficult and requires a lengthy "trial-and-error" construction program. Also, most composites tend to absorb water which could compromise its thermomechanical properties. Both of these issues could significantly increase resonator construction costs.

VI. Preliminary Design for a Microwave Spectrometer

A. Resonator Design

The previous analyses led to the recommendation that a single-mode, confocal, or semi-confocal Fabry-Perot resonator be employed for determining the absorptivity of atmospheric gases. This section will evaluate the performance and accuracy of a specific resonator design. These analyses are intended to demonstrate the feasibility of resonator absorption measurements, clarify details that need to be resolved in the next phase of design studies, and provide the basis for estimating resources required for completing a measurement program.

A preliminary resonator design is depicted in Figure 8. It shows a spherical and a flat mirror mounted on an invar frame. The semi-confocal geometry was chosen over the confocal geometry because it is cheaper to fabricate and easier to align. Between the frame and the flat mirror are shims for athermalizing the structure. The invar frame will be mounted inside an enviromental chamber which is instrumented with temperature, humidity, and pressure sensors.

The resonator Q is determined by the sum of four terms representing losses resulting from diffraction and imperfect mirror shape, mirror reflectivity, radiation through coupling apertures, and absorption by the internal medium. Equation 55 describes the Q_i associated with finite mirror reflectivity. A gold plated mirror (preferred because it won't oxidize) has a Q_i of 2.7×10^6 at 18 GHz, assuming the internal medium has an intrinsic impedance of 377 Ω. The signal coupler should be designed to produce losses that are a tenth of the reflectivity loss, yielding a Q_r of 27×10^6. At 18 GHz, a 25 cm mirror diameter yields a Fresnel number of 1.2 resulting in diffractive losses roughly 1/8 of the reflectivity losses for a Q_D of 22×10^6. To achieve the same Q with a confocal system would require two 21 cm mirrors. Then Equation 52 shows the Q of the evacuated resonator is 2.2×10^6 at 18 GHz, with a resonance bandwidth of 8 kHz.

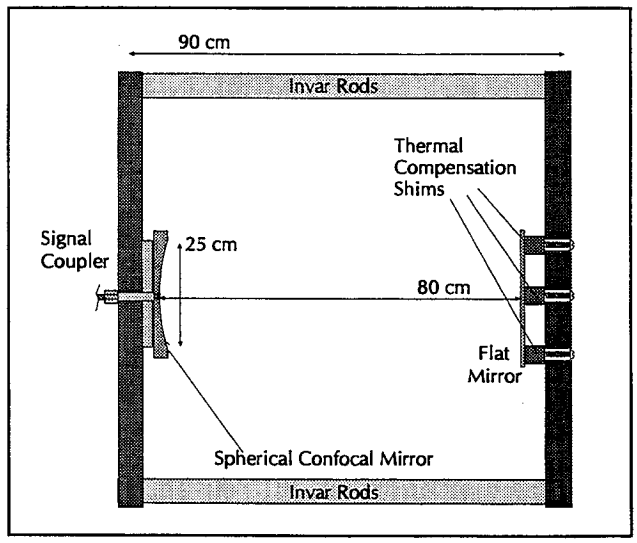

Figure 8. *Preliminary Semi-confocal Resonator Design*

These estimates of diffraction loss are approximate; to precisely determine the appropriate mirror size requires modeling the full resonator with electromagnetic code. Since the dominant loss mechanism is mirror reflectivity loss, which decreases as the square root of frequency, the resonator Q should increase with frequency. At 35 GHz it is 2.9×10^6.

Since Q specifies the total energy loss per reflection, it can be used to calculate an effective path length, l_{eff}, which is a figure of merit representing the mean distance a signal will propagate before it is absorbed or radiated outside the cavity,

$$l_{eff} = \frac{Q\lambda}{2\pi} \quad . \tag{87}$$

This corresponds to the length required for a one-pass absorption cell to have the same performance as the resonator [21]. At 18 GHz, the proposed resonator has an effective length of 6 kilometers, and at 40 GHz the effective length is 4 km.

The resonator eigenfrequencies can be calculated from Equation 50. The $TEM_{0,0,p}$ modes have frequencies $f_{0,0,p} = 94(2p+1)$ MHz, giving a free spectral range of ~190 MHz. The expected frequency detuning for a change in resonator length is 230 MHz/cm at 18 GHz, so a one nanometer change in resonator length will change the resonator frequency by 22.5 Hz. Equation 58 gives the change in Q with respect to a change in resonator length. Assuming broadband coupling (so $d\alpha_t/df$ is small) the change in Q is -6×10^4 per cm. Since Q determines the resonance bandwidth Δf, ($Q = f_c / \Delta f$), the change in bandwidth with cavity length is 100 Hz/cm.

Equations 85 and 86 give the athermalization requirements for the frame's 90 cm invar rods. Roughly three centimeters of aluminum shims are required to compensate for the thermal expansion coefficient of invar. As stated earlier the actual shim width must be determined experimentally.

B. Environmental Control

Environmental control system operating parameters can be estimated from the resonator design. Analyses of the vacuum system capacity and thermal mass helps identify important design issues.

The capacity of the environmental control system is determined by the vacuum chamber volume. A resonator with 25 cm mirrors spaced 80 cm apart would fit comfortably inside a cylindrical vacuum chamber that is a meter in length and 80 cm in diameter. A chamber whose diameter is much greater than that of the resonator is needed both to furnish space for the environmental sensors and to minimize RF coupling of the vacuum chamber and sensors with the resonator. The chamber volume would then be $\pi r^2 L$ or 0.5 m^3 or 500 liters. The time required to evacuate the vacuum chamber can be calculated from Equation 65. Assuming a mechanical roughing pump with moderate capacity (200 liters/minute) it would take slightly less than 20 minutes to pump the vacuum chamber from ambient pressure to below 0.1 kPa.

The system heat capacity can also be estimated. Table 1 gives a crude physical model for the resonator and vacuum chamber. The density and specific heats of the various materials are taken from Table 3 in appendix A. A 20% margin is included to account for the environmental sensors, cables, windows, vacuum couplers, etc. As is indicated in the table, the total mass for the resonator and chamber is 500 kg. Heat capacity is calculated from the specific heat and mass of each component. A somewhat arbitrary value of 500 J/kg-°C was chosen to represent the mix of materials that compose the margin. The total heat capacity of the vacuum chamber and resonator is roughly 2.4×10^5 J/°C. Assuming no heat leaks, 400 watts is needed to raise the temperature of the chamber and resonator 1 °C in 10 minutes. But it is unrealistic to assume no heat leaks, so the actual power needed to achieve this temporal performance is somewhat greater. Since the vacuum chamber comprises the majority of the system thermal mass, accurate control of the vacuum chamber temperature will insure the temperature stability of the resonator. The chamber must be insulated to achieve temperature uniformity. The combination of insulation, chamber thermal mass, and thermal conductivity will minimize temperature drifts in the resonator structure. An effective strategy for data acquisition is suggested by the thermal analysis. Performing each data run or cavity cycle at a set temperature with varying pressures, humidities, and microwave frequencies is most efficient because changing the chamber temperature requires considerably more time than changing these other parameters.

Table 1. Simple Physical Model for the Cavity Resonator and Vacuum Chamber

Description	Dimensions	Material	Mass (kg)	Heat Capacity
Atmospheric Gas	500 liters	Air	0.65 (STP)	0.06×10^4 J/°C
Mirror Supports	4 × 60 cm × 2 cm × 2 cm	Aluminum	3	0.3×10^4 J/°C
Invar Spacers	3 × 80 cm × 5 cm dia. rod	Invar	38	1.7×10^4 J/°C
Spherical Mirror	25 cm dia., 3 cm thick	Aluminum	4	0.4×10^4 J/°C
Flat Mirror	28 cm dia., 0.5 cm thick	Aluminum	1	0.9×10^4 J/°C
Chamber Cylinder	1 m × 82 cm OD, 1 cm wall	Steel	204	9.4×10^4 J/°C
Chamber End Caps	2 × 82 cm dia., 2 cm thick	Steel	170	7.8×10^4 J/°C
Misc. (Margin)	20% of total mass	Mixed	84	3.9×10^4 J/°C
Total			505 kg	24×10^4 J/°C

Since the vacuum chamber is responsible for more than 70% of the mass and heat capacity, large gains can be achieved by reducing the chamber size. This model assumes an 80 cm diameter chamber for a 25 cm diameter confocal Fabry-Perot resonator. The large difference in diameters is driven primarily by the need to minimize electrical coupling between the vacuum chamber walls and the resonator. However, that chamber diameter may be excessive. This provides an important incentive for developing a sophisticated computer model to analyze resonator-chamber

coupling using commercial electromagnetic simulation software. It may also be possible to reduce the environmental chamber size by coating it with an epoxy-based absorber. If the vacuum chamber diameter can be reduced 10 cm without significantly impacting the electrical performance of the resonator, then its mass will drop by 66 kg and the heat capacity by 3×10^4 J/°C.

C. Assessment of Resonator Accuracy

Refraction and absorption measurement errors are introduced by uncertainties in frequency measurement, deformations in the resonator structure, and inaccurate measurement and control of the gas sample's thermodynamic state. The accuracy to which resonator bandwidth Δf and center frequency f_c can be measured is a function of resonator Q, integration time, and stability of the RF electronics. Thermal fluctuations and mechanical vibration can deform or warp the resonator structure causing potentially significant measurement uncertainties. Errors in the gas sample temperature, chamber humidity or pressure, and unmeasured variations in the thermodynamic properties will introduce errors in absorption and refraction determinations. The central problem is to identify sources of systematic errors because random errors can be reduced by averaging.

Resonator bandwidth and center frequency measurement accuracy is investigated in section IV.G. The worst-case error that can be incurred during determination of refractivity from a single pair of center frequency measurements is given by Equation 72. Calculations of the proposed resonator show that for a range of 18 to 35 GHz, refractivities spanning 100 ppm (mid-troposphere, ~9 km) to 400 ppm (humid sea level) with a 250 msec integration time incur refractivity errors $\Delta N/N$ ranging from 1.2×10^{-6} to 7×10^{-8}. The worst-case error for an absorptivity determination is given by Equation 77. For 250 msec integration time and 18 to 35 GHz, the worst-case accuracy ranges from 3.2×10^{-3} to 4.0×10^{-3} dB/km.

Deformations in the resonator geometry due to thermal expansion or mechanical vibration can cause significant errors in refractivity and absorptivity measurements. This is primarily due to the sensitivity of resonance center frequency to resonator length. Refractivity measurements are most sensitive to uncompensated center frequency drifts over longer time scales, specifically the time period between loaded measurements and vacuum measurements. If the difference in chamber temperatures can be measured to within 0.1 °C the effects of thermal drift can largely be removed from calculated refractivities. Frequency errors due to vibrations tend to average out because the time scale is long with respect to the period of vibrations and thus should not be of significance.

Absorptivity measurements are most sensitive to frequency drifts on much shorter time scales, the time between measurement of f^+ and f^-, and this makes them sensitive to short term frequency drift rates. Various sources of drift may cause correlated or anticorrelated errors in f^+ and f^-. For example, thermal expansion of the resonator structure can cause systematic biases in bandwidth measurements that yield absorptivities. Errors in the thickness of compensating shims discussed earlier can yield frequency drifts as the resonator temperature changes. Assuming

90 cm invar spacing rods with 3.4 cm aluminum compensation shims, a 0.5-mm error in shim thickness yields a temperature sensitivity of 12 nm/°C. Thus a temperature change of 0.1 °C will cause a 1.2 nm length change. Using the frequency sensitivity calculated in section VI.A, 230 MHz/cm at 18 GHz, a 1.2 nm length change causes a 27 Hz center frequency change. If the change occurs in the time between measurement of f^+ and f^-, on the order of 1 second, it causes a 27 Hz error in the bandwidth measurement. This is the same order of magnitude as the estimated frequency measurement error. The large thermal capacity of the system will ensure that thermal drift rates are much smaller than 0.1 °C/sec, so bandwidth measurement errors due to thermal drift will be smaller than the innate frequency measurement uncertainties.

Vibration-induced deformations are more difficult to quantify than thermal deformations. The vacuum chamber design should incorporate passive vibration isolation such as rubber cushioned floor mounts. However, the need for greater isolation can only be determined by direct measurement. Vibration-induced frequency variations can be distinguished from the other sources by comparing the time series and spectra of frequency variations with concurrent time series and spectra of mechanical noise measured independently with a transducer.

Environmental measurement and control accuracy sets limits on the accuracy of the absorptivity and refractivity. Pressure and temperature can be measured with sufficient accuracy to make their contribution to the overall error budget insignificant. This is in contrast with humidity which can be measured with an accuracy of 0.5% to 1.0% over the relevant thermodynamic range of interest. Therefore, additional effort expended in improving the accuracy of techniques for measuring water vapor content would yield significant improvements in absorption and refraction accuracy. Accurate control of temperature and humidity is also crucial to making accurate measurements. Several error sources are sensitive to temperature variations and a thermal design which helps stabilize the resonator temperature would reduce the total error budget. Stable humidity during the measurement period would also decrease the total error.

The experimental systems will need to be "tuned" to achieve the requisite level of accuracy. Diagnostics are necessary to insure that the vibration, temperature, and frequency measurement errors are random rather than systematic. As discussed earlier, assumptions regarding randomness of resonator measurement errors need to be verified. Since the refractivity of nitrogen, argon, and oxygen are independently known to 0.1%, they provide a calibration standard. Repeated refractivity measurements on these gases will allow compilation of statistics on total measurement accuracy and provide diagnostic on the various sources of measurement error. Also, bandwidth measurements on listless gases such as argon and nitrogen, as well as the evacuated resonator can reveal systematic anticorrelations during measurement of the -3 dB power points. These two types of measurements will allow the randomness of the errors to be tested to 0.1% or better. They will also allow investigation of systematic changes in cavity bandwidth and center frequency as a function of pressure, internal medium, and frequency to the 0.1% level or better. These tests will provide the information necessary to drive the total multiple-measurement error down to the 0.1% level.

It has been pointed out (R. Linfield, pers. comm.) that the deep space applications only require a relationship between emission and refraction and do not actually require accurate determination of water vapor content. This study suggests that although we need all the accuracy that can be obtained from environmental measurements for diagnostic reasons, the use of refractivity measurements in lieu of accurate water vapor and temperature measurements could possibly be improved by a factor of two or three by analysis which directly connects refractivity to absorptivity. This limit is set by the total instrumental error floor of ~0.1%, the non-unique mapping between water vapor content and refractivity, and the need for water vapor measurements as a diagnostic. Therefore, refractivity errors can be potentially traded off with water vapor measurement errors to reduce the total error to 0.3% to 0.6%.

In conclusion, the critical tasks which determine absorption and refractivity accuracy are resonator temperature control, water vapor measurement accuracy, and dry gas measurement calibration. Resonator measurements of dry gas refractivity allow systematic errors to be diagnosed to 0.1%. The primary source of error in absorptivity and refractivity measurements is thus the ability to measure the concentration of water vapor in the resonator path. Over the whole thermodynamic range of interest, the accuracy of water vapor measurement is 1.5%. However, over the thermodynamic range responsible for most of the radio delay (i.e., conditions in the bottom two kilometers of the atmosphere), the accuracy of water vapor measurements ranges from 0.5% to 1.0%. The use of a direct association between refractivity and absorptivity which does not use humidity measurements may decrease the total error to 0.3% - 0.6%. Therefore the overall absolute accuracy of resonator-based absorption and refractivity measurements ranges from 0.5% to 1.0% with a precision of 0.3% or better.

D. Recommendations for Laboratory Measurements Program

This feasibility study is the first step towards developing a microwave spectrometer to determine atmospheric absorption coefficients. Realization of improved accuracy will require a detailed design, spectrometer construction, instrumental testing, measurements on atmospheric gases, data analysis, and spectral modeling. This section will highlight technical issues that need to be addressed. This will provide a framework for scheduling and estimating costs. Although it is inappropriate to project costs and timetables in this document, they are available upon request.

The goal of a phase II design study is to generate detailed mechanical and electronic drawings for fabricating the resonator, environmental control system, measurement electronics, and data acquisition system. Central to the resonator design is use of electromagnetic simulation code to model the resonator structure and environmental probes to ensure that they do not significantly affect resonator Q. Using the electromagnetic code it is worth examining possible benefits from a nonconfocal mirror spacing. By reducing the ratio of mirror spacing to mirror radius of curvature the mode spacing changes potentially significantly reducing overlap between modes. Also critical to achieving a high Q is development of a low-loss, broadband coupling probe. Measurement electronics and the data acquisition system do not pose significant technical challenges, but their design should be developed to a point where procurements can be placed. The environmental control system needs specific emphasis placed on thermal performance,

environmental sensing, and gas delivery system analysis. Stabilizing the environmental chamber temperature is critical to ensuring accurate interpretation of absorption measurements. A design which minimizes the time it takes to change the chamber temperature is important because it will reduce the pre-measurement setup time. Additional investigation is needed to select the appropriate technologies for monitoring humidity, pressure, and temperature inside the environmental chamber. The gas delivery system requires thorough analysis to determine the optimum number of humidifiers and specifications for the heat exchangers. Gas pressures and flow rates should be calculated through the whole delivery system to ensure that appropriate flow rates can be produced and expansion in the humidifiers does not limit the potential range of humidities. Finally, the design should be sufficiently detailed to allow procurement to begin.

The next stage of a measurement program would be construction. This begins with procurements and drafting machine shop work orders which makes this the most costly phase. Scheduling and cost estimates need to consider construction of the resonator, vacuum chamber, environmental sensors, vacuum system, gas delivery system, measurement electronics, and data acquisition system. Also, at this point, laboratory space is needed. This phase will result in an operating spectrometer.

Spectrometer testing and validation overlaps the construction phase. Various subsystems require evaluation. The vacuum system and environmental chamber must be checked for leaks. Gas delivery and humidity controls require testing and demonstration. Thermal compensation of the resonator structure needs to be tuned to minimize the resonator thermal expansion coefficient. The RF electronics must be checked to ensure that their operating characteristics are stable. The microwave signal coupler will need calibration. The conditions which induce the onset of vapor condensation should be quantified and possible mitigation measures tested. Responses of the various temperature control servos also need verification. Finally, after the spectrometer is fully characterized the measurement phase can begin.

Absorption measurements will be made concurrently with the data analysis. This phase will start with dry nitrogen calibrations followed by dry air measurements. During these initial measurements, a data taking strategy will develop which will serve as a model for the duration of the data acquisition period. By the end of this phase, measurements will be made over the specified range of humidities, pressures, and temperatures. Some repetition will be warranted to help quantify the measurement uncertainty. A minimum of six months will be needed to span the full thermodynamic range for all RF frequencies of interest.

Finally, the data will be used to construct a new absorption model. Measurements made over the specified thermodynamic range will allow current representations of temperature, pressure, and humidity dependence to be verified. Finally, the whole data set will be fit to an *a priori* spectral model to generate the new high-accuracy water vapor model.

E. Conclusion

A preliminary design study examined the feasibility of using microwave resonator measurements to improve the accuracy of atmospheric absorption coefficients and refractivity between 18 and 35 GHz. Increased accuracies would improve the capability of water vapor radiometers to correct for radio signal delays caused by Earth's atmosphere. Calibration of delays incurred by radio signals traversing the atmosphere has applications to deep space tracking, VLBI, and planetary radio science experiments. The primary beneficiary of enhanced atmospheric calibration is the Cassini Radio Science gravity wave search which requires 0.8-1.0% absorption coefficient accuracy.

This study examined current atmospheric absorption models and estimated that current model accuracy ranges from 5% to 7%. The refractivity of water vapor is only known to 1% accuracy, while the refractivity of many dry gases (oxygen, nitrogen, etc.) are known to better than 0.1%. Improvements to the current generation of models will require that both the functional form and absolute absorption of the water vapor spectrum be calibrated and validated.

Several laboratory techniques for measuring atmospheric absorption and refractivity were investigated including absorption cells, single and multimode rectangular cavity resonators, and Fabry-Perot resonators. Absorption cells did not provide sufficient signal to accurately determine the absorptivity of weakly absorbing atmospheric gases. Multimode cavity resonator measurements such as those performed by Becker and Autler several decades ago were shown to lack diagnostics necessary to control the various sources of systematic errors to the 1% level. Comparisons between single-mode rectangular cavity resonators and Fabry Perot resonators indicate that to achieve the same performance the rectangular cavity requires more than eight times the volume of an equivalent Fabry-Perot. It was concluded that the semi-confocal Fabry-Perot resonator provides the most cost-effective and accurate method of measuring atmospheric gas refractivity.

The need for accurate environmental measurement and control was also addressed. The thermodynamic state of the sample gas (i.e., pressure, humidity, and temperature) limits the accuracy of the absorption and refraction measurements. In fact, it was shown that accurate thermal control of the vacuum chamber is critical to controlling a number of systematic error sources. A preliminary design for the environmental control and measurement system was developed to aid in identifying significant design issues and to allow costing of its construction.

The analysis indicated that overall measurement accuracy will be limited by measurement errors and imprecise control of the gas sample's thermodynamic state, thermal expansion and vibration-induced deformation of the resonator structure, and electronic measurement error. Uncertainties in electronic methods for measuring the resonator bandwidth and center frequency were analyzed. Methods for compensating the resonator structure for thermal expansion and identifying systematic errors introduced by vibration were also explored. The central problem is to identify systematic errors because random errors can be reduced by averaging. Calibrating the resonator measurements by checking the refractivity of dry gases which are known to better than 0.1%

provides a method of controlling the systematic errors to 0.1%. The primary source of error in determining the accuracy of absorptivity and refractivity measurements is thus the ability to measure the amount or concentration of water vapor in the resonator path. Over the whole thermodynamic range of interest the accuracy of water vapor measurements is 1.5%. However, over the thermodynamic range responsible for most of the radio delay (i.e., conditions in the bottom two kilometers of the atmosphere) the accuracy of water vapor measurements ranges from 0.5% to 1.0%. Therefore the precision of the resonator measurements could be held to 0.3% and the overall absolute accuracy of resonator-based absorption and refractivity measurements will range from 0.6% to 1.1%.

We would like to acknowledge Herb Pickett, Stephen Keihm, MJ Mahoney, George Resch, and Roger Linfield for their helpful comments and suggestions. This research was funded under the DSN Technology and Science Office. The research described in this report was carried out by the Jet Propulsion Laboratory, California Institute of Technology, under a contract with the National Aeronautic and Space Administration.

Appendix A. Material Properties

The conductivity of the mirror surfaces determine their loss. The conductivity, skin depth, and surface resisitivity of various materials are listed in Table 2. Frequency, f, should be specified in Hertz.

Table 2. Electrical Properties of Various Materials

Material	Conductivity mhos/meter σ	Skin Depth meters δ	Surface Resistivity R_s	Ref
Gold	4.10×10^7	$0.0787\, f^{-1/2}$	$3.10 \times 10^{-7} f^{1/2}$	[66]
Silver	6.17×10^7	$0.0642\, f^{-1/2}$	$2.52 \times 10^{-7} f^{1/2}$	[37]
Copper	5.80×10^7	$0.0660\, f^{-1/2}$	$2.61 \times 10^{-7} f^{1/2}$	[37]
Machine Steel	$0.5-1.0 \times 10^7$	$0.01-0.02\, f^{-1/2}$	$1-1.5 \times 10^{-5} f^{1/2}$	[37]
Aluminum	3.72×10^7	$0.0826\, f^{-1/2}$	$3.26 \times 10^{-7} f^{1/2}$	[37]
Brass (nominal)	1.57×10^7	$0.127\, f^{-1/2}$	$5.01 \times 10^{-7} f^{1/2}$	[37]
Solder (nominal)	0.706×10^7	$0.185\, f^{-1/2}$	$7.73 \times 10^{-7} f^{1/2}$	[37]
Water (distilled)	2×10^{-4}	$4 \times 10^4 f^{-1/2}$	$10^{-1} f^{1/2}$	[66]
Water (fresh)	10^{-3}	$2 \times 10^4 f^{-1/2}$	$6 \times 10^{-2} f^{1/2}$	[66]
Sea Water	3-5	$2-4 \times 10^2 f^{-1/2}$	$10^{-3} f^{1/2}$	[66]

The thermal properties of the materials used to construct a resonator affect its performance and operational specifications. Table 3 gives a list of materials that are relevant to resonator design.

Table 3. Thermal Properties of Various Materials

Material	Thermal Expansion Coefficient, α, ($^{\circ}C^{-1}$)	Density, ρ, (kg/m^3)	Thermal Conductivity W/(m-°C)	Specific Heat, c_ρ, (J/kg-°C)
Ice	51×10^{-6} [65]	0.92×10^3 [68]	1.6 [58]	21×10^2 [69]
Aluminum	24×10^{-6} [67]	2.7×10^3 [69]	200 [68]	8.9×10^2 [68]
Brass	19×10^{-6} [65]	8.5×10^3 [68]	110 [68]	3.8×10^2 [68]
Steel	11×10^{-6} [65]	8.0×10^3 [68]	53 [68]	4.6×10^2 [68]
Invar	0.9×10^{-6} [67]	8.1×10^3 [68]	11 [68]	4.6×10^2 [68]
Copper	51×10^{-6} [67]	8.9×10^3 [68]	390 [68]	3.9×10^2 [68]
Glass (ordinary)	$4-9 \times 10^{-6}$ [67]	2.6×10^3 [69]	0.8 [68]	8×10^2 [69]
Graphite	7.9×10^{-6} [65]	0.40×10^{-3} [69]	- - -	8.6×10^2 [69]
Pyrex	3.2×10^{-6} [67]	2.6×10^{-3} [69]	0.8 [68]	8×10^2 [69]
Quartz (fused)	0.4×10^{-6} [67]	2.6×10^{-3} [69]	- - -	8×10^2 [69]
Air	3.6×10^{-3} [65]†	1.3 [57]	0.024 [68]	10×10^2 [68]

† Volume expansion coefficient at STP.

Bibliography

[1] Elgered, G., Atmospheric Remote Sensing by Microwave Radiometry, 215-258, John Wiley & Sons, 1993.

[2] Linfield, R., et al. (TDA), OSC Advanced System Review, DSN Advanced Systems, JPL, Pasadena, CA, June 15-18, 1993 (internal document).

[3] Spilker, T.R., "Laboratory Measurements of Microwave Absorptivity and Refractivity Spectra of Gas Mixtures Applicable to Giant Planet Atmospheres," Stanford Univ., Ph. D. dissertation, 1990.

[4] Becker, G.E., and S.H. Autler, Phys. Rev., 70, 300-307, 1946.

[5] Riley, A.L., et al., Cassini Ka-band precision Doppler and enhanced telecommunications system study, JPL - Agenzia Spaziale Italiana report, January 22, 1990.

[6] Dolinsky, S., Cassini Ka-Band Radio Science Study (DSS 13 Option), JPL TDA Office 430, Pasadena, CA, August 1992 (internal document).

[7] Keihm, S.J., Preliminary WVR wet path delay corrections for the 4/22/93 VLBI experiment for Goldstone, JPL IOM 3833-93-261, June 7, 1993 (internal document).

[8] Westwater, E. R., J. B. Snider, M. Falls, Observations of atmospheric emission and attenuation at 20.6, 31.65, and 90 GHz by a ground-based radiometer, NOAA Technical Memorandum ERL WPL-156, November 1988.

[9] De Lucia, F.C., P. Helminger, and W. Kirchhoff, Microwave spectra of molecules of astrophysical interest, V. Water Vapor, J. Phys. Chem. Ref. Data, 3, 211-219, 1974.

[10] Townes C.H., and A.L. Schawlow, Microwave Spectroscopy, McGraw-Hill, New York, 1955.

[11] Rosenkranz, P.W., Interference coefficients for overlapping oxygen lines in air, J. Quant. Spectrosc. Radiat. Transfer, 39, 287-297, 1988.

[12] Van Vleck, J.H., The absorption of microwaves by oxygen, Phys. Rev., 71, 413-424, 1947.

[13] Gross E.P., Shape of collision-broadened spectral lines, Phys. Rev., 97, 395-403, 1955.

[14] Van Vleck, J.H. and V.F. Weisskopf, On the shape of collisionally broadened lines, Rev. Mod. Phys., 17, 227-236, 1945.

[15] Walter, S.J., "Tropospheric Water Vapor Microwave Spectrum: Uncertainties for Remote Sensing," S. Walter, Proceedings of the Specialist meeting on Microwave Radiometry and Remote Sensing Applications, Boulder, CO, January, 1992.

[16] Lam, K.S., Application of pressure broadening theory to the calculation of atmospheric oxygen and water vapor microwave absorption, J. Quant. Spectrosc. Radiat. Transfer, 17, 351-383, 1977.

[17] Ben-Reuven, A., Impact broadening of microwave spectra, Phys. Rev., 145, 7-22, 1966.

[18] Ben-Reuven, A., Transition from resonant to nonresonant line shape in microwave absorption, Phys. Rev. Lett., 14, 349-351, 1965.

[19] Ben-Reuven, A., The meaning of collision broadening of spectral lines: the classical-oscillator analog, Adv. At. Mol. Phys., 5, 201-235, 1969.

[20] Liebe, H.J. and D.H. Layton, Millimeter-wave properties of the atmosphere: laboratory studies and propagation modeling, NTIA Report 87-224, U.S. Department of Commerce, 1987.

[21] Liebe, H.J., P.W. Rosenkranz, and G.A. Hufford, Atmospheric 60-GHz oxygen spectrum: New laboratory measurements and line parameters, J. Quant. Spectrosc. Radiat. Transfer, 48, 629-643, 1992.

[22] Burch, D.E. and D.A. Gryvnak, Atmos. Water Vapor, Proc. Int. Wkshp on Atmos. Water Vapor, Vail, CO, Sept 11-13, 1979, 47-76, Academic, New York, 1980.

[23] Hinderling, J., M.W. Sigrist, and F.K. Kneubuhl, Laser-photoacoustic spectroscopy of water-vapor continuum and line absoprtion in the 8 to 14 μm atmospheric window, Infrared Phys., 27, 66-120, 1987.

[24] Clough, S.A., F.X. Kneizys, R. Davies, R. Gamache, and R. Tipping, Theoretical line shape for H_2O vapor, applications to the continuum, Atmospheric Water Vapor, Proceedings of Int. Workshop on Atmospheric Water Vapor, Vail, CO, Sept 11-13, 1979, 25-46, Academic, New York, 1980.

[25] Ma, Q. and H. Tipping, Water vapor continuum in the millimeter spectral region, J. Chem. Phys., 93, 6127-6138, 1990.

[26] Ma, Q. and H. Tipping, The atmospheric water continuum in the infrared: Extension of the statistical theory of Rosenkranz, J. Chem. Phys., 93, 7066-7075, 1990.

[27] Carlon, H.R., Do clusters contribute to the infrared absoption spectrum of water vapor? Infrared Phys., 19, 549-557, 1979.

[28] Gebbie, H.A., Observations of anomalous absorption in the atmosphere, Atmospheric Water Vapor, Proceedings of Int. Workshop on Atmospheric Water Vapor, Vail, CO, Sept 11-13, 1979, 133-142, Academic, New York, 1980.

[29] Bohlander, R.A., R.J. Emery, D.T. Llewellyn-Jones, G.G. Gimmestad, H.A. Gebbie, O.A. Simpson, J.J. Gallagher, and S. Perkowitz, Excess absorption by water vapor and comparison with theoretical dimer absorption, Atmospheric Water Vapor, Proceedings of Int. Workshop on Atmospheric Water Vapor, Vail, CO, Sept. 11-13, 1979, 241-254, Academic, New York, 1980.

[30] Buffey, I.P. and W.B. Brown, A theoretical study of the infrared absorption spectra of large water clusters, J. Chem. Soc. Faraday Trans., 86, 2357-2360, 1990.

[31] Hudis, E., Y. Ben-Aryeh, and U.P. Oppenhiem, The contribution of third order linear absorption to the water vapor continuum, J. Quant. Spectrosc. Radiat. Transfer, 47, 319-323, 1992.

[32] Hudis, E., Y. Ben-Aryeh, and U.P. Oppenhiem, Third order linear absorption by pairs of molecules, Phys. Rev. A, 43, 3631-3639, 1992.

[33] Hill, R.J., R.S. Lawrence, and J.T. Priestley, Theoretical and calculational aspects of the radio refractive index of water vapor, Radio Sci., 17, 1251-1257, 1982.

[34] Owens, J.C., Optical refractive index of air: dependence on pressure, temperature, and composition, Appl. Opt., 6, 58-59, 1967.

[35] Van Vleck, J.H., The Theory of Electric and Magnetic Susceptibilities, Oxford Univ. Press, 1932.

[36] Newell, A.C. and R.C. Baird, Absolute determination of refractive indices of gases at 47.7 gigahertz, Journal of Applied Physics, 36, 3751-3759, 1965.

[37] Boudouris, G., On the index of refraction of air, the absorption and dispersion of centimeter waves by gases, J. Res. Nat. Bur. Stand. Sec. D, 67, 631-684, 1963.

[38] Bean, B.R. and E.J. Dutton, Radio Meteorology, Dover, New York, 1968.

[39] Walter, S.J., "Measurement of the microwave propagation delay induced by atmospheric water vapor," Univ. of Colorado, Ph.D. Dissertation, 1990.
[40] Liebe, H.J. and G.G. Gimmestadt, Calculation of clear air refractivity, Radio Sci., 20, 245-251, 1978.
[41] 1994 Test & Measurement Catalog, Hewlett-Packard Company, San Francisco, CA, 1993.
[42] Donecker, B., Determining the measurement accuracy of the HP 8510 microwave network analyzer, RF & Microwave Measurement Symposium and Exhibition, Hewlett-Packard, March 1985.
[43] Reitz, J.R., F.J. Milford, and R.W. Christy, Foundations of Electromagnetic Theory, 3rd Ed., Addison Wesley, 1979.
[44] Ramo, S., J.R. Whinnery, and T. Van Duzer, Fields and waves in communication electronics, John Wiley & Sons, New York, 1965.
[45] Spilker, T.R., New laboratory measurements on ammonia's inversion spectrum, with implications for planetary atmospheres, JGR-Planets, 98E, 5539-5548, 1993.
[46] Jackson, J.D., Classical electrodynamics, 2nd Ed., Wiley & Sons, New York, 1975.
[47] Collin, R.E., Foundations in Microwave Engineering, McGraw-Hill, 1966.
[48] Montgomery, C.G., Technique of Microwave Measurements, McGraw-Hill, New York, 1947.
[49] Boyd, G.D., and J.P. Gordon, Confocal multimode resonator for millimeter through optical wavelength masers, Bell System Tech. Jour., 489-508, March 1961.
[50] Hecht, E. and A. Zajac, Optics, Addison Wesley Publishing Company, Menlo Park, 1974.
[51] Fox, A.G. and T. Li, Resonant Modes in a Maser Interferometer, The Bell System Technical Journal, March 1961.
[52] Lichtenstein, M., J.J. Gallagher, and R.E. Cupp, Millimeter spectrometer using a Fabry-Perot Interferometer, Rev. Sci. Instru., 34, 843-846, Aug. 1963.
[53] Kogelnik, H. and T. Li, Laser Beams and Resonators, Proc. of IEEE, 154, October 1966.
[54] Lamb, W.E., Theory of a microwave spectroscope, Phys. Rev., 70, 308-317, 1946.
[55] NIST Calibration Services User Guide, NIST Special Publication No. 250, Revised October 1991.
[56] Liebe, H.J., V.L. Wolfe, and D.A. Howe, Test of wall coatings for controlled moist experiments, Rev. Sci. Instrum., 55, 1702-1705, October 1984.
[57] Hardy, B., Two Pressure Humidity Calibration on the factory floor, Sensors, 15-18, July 1992.
[58] Turnbull, A.H., R.S. Barton, and J.C. Riviere, An introduction to vacuum techniques, John Wiley & Sons, Great Britain, 1962.
[59] Vacuum Components and Leak Detectors, 1993-1994 Catalog, Veeco Instruments Inc., Plainview, N.Y. 1993.
[60] Matheson Gases & Equipment, 1993 Catalog, Matheson Gas Equipment Technology Group.
[61] Pryde, L.T., Environmental Chemistry, An Introduction, Cummings, Menlo Park, CA, 1973.
[62] Greenspan, L., Functional equations for the enhancement factors for CO_2-free air, Jour. of Res. Nat Bur. of Stand., 80A, 41-44, 1976.

[63] Wexler, A., R.W. Hyland, S. Hasegawa, and P.H. Huang, NIST Calibration Services for Humidity Measurement, NIST Internal Report # 4677, October, 1991.
[64] Hasegawa, S. and J. W. Little, The NBS two-pressure humidity generator: Mark 2, Jour. of Res. Nat Bur. of Stand., 81A, 81-88, 1976.
[65] Tipler, P.A., Physics, 1st Ed., Worth Publishers, Inc., New York, 1976.
[66] Seshadri, S.R., Transmission Lines and Electromagnetic Fields, Addison Wesley, Phillipines, 1971.
[67] Sears, F.W., M.W. Zemansky, and H.D. Young, University Physics, 6th Ed., Addison Wesley, Philippines, 1982.
[68] Holman, J.P., Heat Transfer, 3rd Ed., McGraw-Hill Books, New York, 1972.
[69] Oberg, E., F.D. Jones, and H.L. Horton, Machinery's Handbook Guide, 23rd Ed., Industrial Press, Inc., New York, 1988.